Master's thesis
Materials Research
Computational Materials Physics

Interatomic potential for molecular dynamics simulations of radiation effects in WMoTa concentrated alloys

Juuso Kauppala

7.2.2021

Supervisor(s): Flyura Djurabekova
Jesper Byggmästar

Examiner(s): Flyura Djurabekova
Jesper Byggmästar

University of Helsinki
Faculty of Science
PL 64 (Gustaf Hällströmin katu 2a)
00014 Helsingin yliopisto

HELSINGIN YLIOPISTO — HELSINGFORS UNIVERSITET — UNIVERSITY OF HELSINKI

Tiedekunta — Fakultet — Faculty	Koulutusohjelma — Utbildningsprogram — Degree programme
Faculty of Science	Materials Research Computational Materials Physics

Tekijä — Författare — Author

Juuso Kauppala

Työn nimi — Arbetets titel — Title

Interatomic potential for molecular dynamics simulations of radiation effects in WMoTa concentrated alloys

Työn laji — Arbetets art — Level	Aika — Datum — Month and year	Sivumäärä — Sidantal — Number of pages
Master's thesis	7.2.2021	57

Tiivistelmä — Referat — Abstract

The rapidly increasing global energy demand has led to the necessity of finding sustainable alternatives for energy production. Fusion power is seen as a promising candidate for efficient and environmentally friendly energy production.

One of the main challenges in the development of fusion power plants is finding suitable materials for the plasma-facing components in the fusion reactor. The plasma-facing components must endure extreme environments with high heat fluxes and exposure to highly energetic ions and neutral particles. So far the most promising materials for the plasma-facing components are tungsten (W) and tungsten-based alloys. A promising class of materials for the plasma-facing components is high-entropy alloys. Many high-entropy alloys have been shown to exhibit high resistance to radiation and other wanted properties for many industrial and high-energy applications.

In materials research, both experimental and computational methods can be used to study the materials' properties and characteristics. Computational methods can be either quantum mechanical calculations, that produce accurate results while being computationally extremely heavy, or more efficient atomistic simulations such as classical molecular dynamics simulations. In molecular dynamics simulations, interatomic potentials are used to describe the interactions between particles and are often analytical functions that can be fitted to the properties of the material. Instead of fixed functional forms, interatomic potentials based on machine learning methods have also been developed. One such framework is the Gaussian approximation potential, which uses Gaussian process regression to estimate the energies of the simulation system.

In this thesis, the current state of fusion reactor development and the research of high-entropy alloys is presented and an overview of the interatomic potentials is given. Gaussian approximation potentials for WMoTa concentrated alloys are developed using different number of sparse training points. A detailed description of the training database is given and the potentials are validated. The developed potentials are shown to give physically reasonable results in terms of certain bulk and surface properties and could be used in atomistic simulations.

Avainsanat — Nyckelord — Keywords

fusion, high-entropy alloy, interatomic potential, molecular dynamics, machine learning potential

Säilytyspaikka — Förvaringsställe — Where deposited

Muita tietoja — Övriga uppgifter — Additional information

Contents

1. Introduction

The rapidly increasing consumption of natural resources and the growing energy demand sets major challenges for energy production technology. Sustainable energy production solutions are needed in order to fulfill the vastly growing global demand [1]. Fusion power provides a promising solution for energy supply with practically inexhaustible natural resources for fuel [2]. To make use of the fusion reaction as a source of energy, durable materials with suitable properties need to be developed for the fusion power plants and their plasma-facing components [3].

The plasma-facing components (PFC) are exposed to harsh environments and have to operate under extreme heat fluxes and exposure to high-energy radiation of neutral particles as well as ions [3]. The requirements for the materials' properties omits the use of a large fraction of the known materials. Tungsten (W) has shown to exhibit wanted characteristics as a PFC material such as a high melting point and strength at high temperatures [4, 5]. Tungsten also has low thermal expansion coefficient, is highly conductive, has a high threshold for sputtering and moderate tritium retention [6]. Although having many promising properties, tungsten suffers from deficiencies as the material used in plasma-facing components: Not only does it have a high brittle-to-ductile transition temperature, but it has also been shown to experience embrittlement due to irradiation [6]. Exposure to helium and deuterium can also cause defects and bubble formation in tungsten at high temperatures [7, 8].

A possible solution for the PFC materials is provided by a fairly new class of materials: High-entropy alloys (HEA) or Complex concentrated alloys (CCA) [9]. Different high-entropy alloys have been shown to exhibit significantly greater radiation resistance than many conventional materials used in applications with harsh environments [10, 11, 12, 13].

In materials research, computational methods can aid in developing predictive models for materials' properties under varying environments. Molecular dynamics simulations (MD) provide a compromise between accuracy and efficiency with respect to other methods such as density functional theory (DFT). However, the accuracy of MD relies heavily on the quality of the interatomic potentials (IAP). Traditional IAPs are parametric models, that are fit to either experimental or computational data to correctly reproduce the properties of the material. The conventional parametric IAPs are unable to make predic-

tions of all properties of the material with high accuracy [14, 15].

A new type of IAP was recently developed based on a machine learning technique called Gaussian process regression: The Gaussian approximation potentials (GAP) [16]. Gaussian approximation potentials have been shown to be able to give predictions with the accuracy close to DFT with much higher efficiency and a GAP was recently developed for W with great results [17].

In this work, the theoretical framework of the GAPs is presented and GAPs for complex concetrated three-elemental alloys (Mo-Ta-W) are developed. The current progress in the research of fusion reactors and HEAs are also reviewed and some classical interatomic potentials are introduced.

2. Materials for fusion applications

2.1 Fusion nuclear power plants as a green alternative for efficient energy production

The vastly growing human population and increasing consumption of natural resources has led to the necessity of finding renewable energy production alternatives. The increasing global demand for energy and the ongoing climate change place grand challenges that need to be addressed. Main current energy production methods use either fossile fuels or suffer from disadvantages as prospective widespread energy solutions, such as wind, solar and fission nuclear power [1]. Harnessing the energy from fusion reactions could provide an environmentally sustainable solution with profuse resources for future generations [18].

In a fusion reactor the expendable energy is produced in fusion reactions, mostly between hydrogen isotopes. In the most common fusion fusion reaction deuterium (D) and tritium (T) react to produce helium (He) and an energetic neutron (n) as

$$\mathrm{D} + \mathrm{T} \rightarrow \mathrm{He} + \mathrm{n} + 17.6\ \mathrm{MeV}. \tag{2.1}$$

The mass energy per nucleon is lower for He than the constituent elements separately and the remainder of the energy is released in the form of kinetic energy of the products [18]. Deuterium is found in ample amounts in seawater but tritium can be produced within the fusion reaction chamber from lithium (Li), since it has a short half-life and is therefore not found from nature. Luckily, both D and Li are common elements on earth and can be easily accessed.

The research for fusion reactors started already in the first half of the 20th century but major global interest arose after the development of the tokamak design: a torus shaped cavity in which magnetic confinement is used to control the extremely hot plasma [18]. One of the first major leaps forward was taken in the 1970s when the decision to develop a larger experimental fusion reactor, later called Joint European Torus (JET), which started its successful operation at the beginning of the 1980s in Oxfordshire, UK [19]. JET was anticipated to be the first fusion power facility to have a fusion energy gain factor, Q, of 1.0 i.e. that it would produce as much energy from the reactions as would

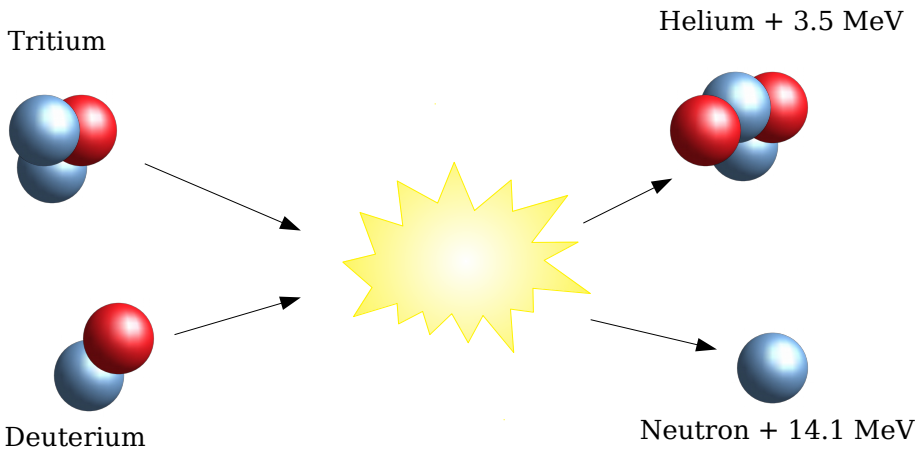

Figure 2.1: A schematic representation of the deuterium-tritium fusion reaction.

be needed to sustain the fusion, but this goal was not reached [2]. Earlier attempts were done using either hydrogen or deuterium but JET was the first facility to operate using a mixture of deuterium and tritium as fuel for the fusion: a schematic image of the reaction is shown in figure 2.1. The maximum Q value of 0.67 was reached in the late 1990s with 24 MW of thermal energy injected to produce 16 MW of fusion energy [2]. JET is still functional and some improvements have been made to the construction over the years, and it has also been used to test concepts from the upcoming large fusion project ITER [20, 3].

A new era in the development of fusion power plants started in the mid 2000s when the International Thermonuclear Experimental Reactor (ITER) was given green light in terms of funding, after which the building of the facility started at Cadarache in France [21]. Originally ITER was planned to be functional by 2020 but is currently still being under construction and the first plasma experiments are expected to be conducted at 2025 [22]. Operating as planned, ITER would be the first fusion reactor to demonstrate that it is indeed possible to produce a surplus in thermal energy by fusion power. The fusion energy gain factor Q would be momentarily 10 so that 50 MW thermal energy fed to the reactor would produce a 500 MW plasma sustained for 400 seconds [20]. This would be achieved by consuming half a gram of deuterium and tritium mixture fuel in the confinement vessel. Still no conversion to electricity of the produced excessive thermal energy is planned since the overall power consuption would still be larger due to the electricity required by the total facility [22]. If no major complications arise ITER will

be the largest plasma physics experiment ever conducted [20] at least until the next generation reactor DEMO starts operating.

The latest and largest current fusion power plant under development is the DEMOnstration Power Station (DEMO) [22, 18]. The conceptual design is still underway but the proposed performance of DEMO should top that of ITER's with fusion energy gain factor $Q = 25$ and thermal output in the range of gigawatts. DEMO is intended to pave way to the first commercial fusion power station designs if the planned performance is reached. So far the schedule of the development of DEMO has been postponed due to changes in the ITER timeline since many of the design concepts from ITER are reused [22].

Although the fuel used in fusion power stations, i.e. hydrogen isotopes, is not truly a renewable source of energy, the extreme availability makes it a practically inexhaustible fountain of thermal energy [18, 2]. Also the output waste of the fusion reaction is inert gas helium in the range of hundreds of kilograms from a fusion power plant producing around 1 GW per year, similarly to the amount of needed fuel. Comparing this to the carbon dioxide (CO_2) waste of fossile fuels using power stations which is in the 10^9 kg, or the radioactive waste of fission power plants with half-life in the range of 10^5 years, fusion power plants appear as a promising candidate for the emerging challenges in global energy production [18].

2.2 Materials in extreme environments for plasma-facing components

The materials of plasma-facing components (PFC) in fusion reactors must endure one of the harshest environments produced by humans: extreme heat fluxes reaching up to several tens of megawatts per square meter (MW/m^2) with energy bursts of megajoules per square meter (MJ/m^2) lasting up to milliseconds alongside with exposure to highly energetic plasma ions and neutral particles such as Deuterium, Tritium, Helium and neutrons [23, 3].

The fusion reaction produces energetic neutrons which will reach the inner walls of the plasma-containing vessel and can produce damage via collision cascades and nuclear transmutations. The exposure to high-energy hydrogen isotopes, D and T, can cause severe embrittlement of the plasma-facing components upon implantation of these particles. Some materials can also form compounds and therefore the chemical composition of the material might be altered [3]. The reaction product helium can also be deposited inside the wall material and can cause blistering, which can in some materials result in quite dramatic changes in the surface structure [24]. Other effects caused by the plasma environments include sputtering erosion, melting and thermal fatigue due to the irradi-

ation and thermal loads. Sputtering not only causes the material to wear but can also contaminate the fusion plasma with the wall material resulting in cooling of the plasma [3].

The most common type of fusion reactor to date is the tokamak magnetic confinement system, in which the plasma containing vacuum vessel is toroidally shaped [2]. In modern reactors, the PFC are composed of so called blanket modules and divertors. Most of the plasma-facing walls are covered with the blankets modules, which transfer heat and serve as protection for the outer components [25]. The bottom part of the confinment vessel is covered with divertor modules, which act as waste collectors inside the reactor. The divertor ensures less contamination by the fusion products or other impurities in the plasma [25].

The PFC materials need to possess certain characteristics, which greatly reduces the possible candidates as materials in PFC and poses one of the biggest challenges in the fusion reactor development [2, 3]. The most commonly used materials in plasma-facing components is beryllium and carbon-fiber composites, yet these suffer from significant drawbacks: beryllium has a melting point of only 1560 K, which is relatively low compared to many other materials. Carbon based materials have been used in the divertor regions, but because of the forming hydrocarbons from the high energy tritium from the plasma, other materials have been examined for the divertor, and so far tungsten based materials seem to have taken the lead [26, 3].

2.3 Tungsten as the main choice for divertors in fusion reactors

The search for the best candidate material in plasma-facing components — specifically in the divertors — of the fusion reactors has ultimately demonstrated tungsten and tungsten based alloys and composites to be the most promising ones [4, 3]. Tungsten has been shown to exhibit many desirable characteristics for these environments having a high melting point (3659 K) as well as other necessary properties: it is hard, has a low thermal expansion coefficient and vapor pressure, high thermal and electrical conductivity and high strength [27]. Many of the wanted properties are also displayed at elevated temperatures [5, 4], which is crucial for fusion reactor applications. In addition tungsten has a high energy threshold for sputtering, moderate tritium retention and low erosion rate [6]. Other materials that are considered have disadvantages due to several reasons such as inadequacy to handle high thermal loads and nuclear transmutations [3].

Yet although tungsten has many essential properties, which make it a prospective material for the divertors, these properties are combined with severe deficiencies. Due

to the electron configuration of tungsten, its ground state is the body-centered cubic lattice, it is brittle at lower temperatures and has a fairly high brittle-to-ductile transition temperature [3, 6]. Another major problem with using elemental tungsten as plasma-facing material is the helium (He) and deuterium (D) induced defects and bubbles at elevated temperatures [28, 7, 8]. Perhaps one of the most crucial issues in using tungsten as plasma-facing material is its tendency for embrittlement due to irradiation [6]. It has been shown that neutron irradiation can cause hardening in tungsten even at fairly low dosages due to voids and dislocation loops, which can also effect the brittle-to-ductile transition temperature [29, 30].

Efforts to circumvent these weaknesses have been made by investigating tungsten-based compounds and binary alloys [3, 31]. To take into account the inherent brittleness of tungsten at lower temperatures, tungsten alloys with elements such as Re, Ta, V, Nb and Mo have been examined but without much improvement [32]. Some improvement over certain properties have been made by binary alloying W with Re, yet many of the issues still retain and alloying with other elements often leads to newer problems [32]. Another suggested method for improving the tungsten-based materials' performance in the high-radiation environment is grain size refinement, which has been shown have an effect on the irradiation-induced defects [33].

The harsh environment, which the plasma-facing components of the fusion reactors need to sustain, sets ample challenges for the development of the fusion power plant materials. For this environmentally friendlier energy with abundant resources to become common practice in the future, an effort to finding the materials that can withstand the required conditions must be exerted. A promising class of materials, which has started to take root in the past decade in the the materials research, has been proposed as an alternative for tungsten: high-entropy alloys. Some of the materials belonging to this class have shown superb mechanical properties even at high temperatures, and promising results in terms of radiation resistance have also been observed. High-entropy alloys could provide suitable candidates for many applications especially in the field of nuclear power in the near future.

3. High-entropy alloys as a new class of materials

3.1 High-entropy alloys

In the past, alloys have generally consisted of one or two principal components with only minor quantities of other elements, which are not necessarily metals. A fairly new class of materials is the so called high-entropy alloys (HEA) that are composed of multiple elements in relatively large fractions [9]. The earliest definition of high-entropy alloys originating from Yeh et al. [34] describes them as multicomponent alloys with at least 5 different elements in concentrations between 5 to 35 atomic percentage, although no universally accepted formal definition exists [35]. At the same time Cantor et al. [36] were investigating multi-component alloys with almost equimolar concentrations, but did not use the term high-entropy alloy. Differing definitions have since then been introduced and research around materials that are comprised of several principal elements has been expanded to a more general class of materials collectively known as complex concentrated alloys (CCA) [9, 37].

One definition also from Yeh categorizes the multicomponent alloys by their ideal mixing entropy values to low-, medium- and high-entropy alloys [38, 39]. Yet this approach holds some issues since the alloy's mixing entropy value might differ even quite drastically with varying temperatures. Another implication of this definition is that the atoms in the lattice acquire random positions and mix completely, which is not necessarily true for certain alloys even in liquid state [38, 37].

Another definition uses the microstructural arrangements as the starting point and says that high-entropy alloys must be single-phase solid solutions [40]. This approach is introduced, since for many of the possible applications, it is necessary for the material to be a single-phase solid solution instead of an intermetallic compound [40, 37]. Although a lot of emphasis has been put on studying single-phase solid solution high-entropy alloys, this definition has not been exclusively accepted either [37, 9].

The research of multi-principal element alloys began already decades before the term

high-entropy alloy was introduced, but broader interest in their development took off after it was noted that a vast space of uninvestigated multicomponent phase space would be within reach and that these materials could have interesting properties [9, 35, 37]. Later research has shown high-entropy alloys and related materials to hold many useful properties for practical applications, some of which seem to be more or less general and others mainly characteristics of certain special cases [37, 41, 35]. General wanted properties possessed by a range of the high-entropy alloys include mechanical properties such as high strength at wide temperature range, high fracture toughness and good corrosion resistance [41, 35, 42, 43]. These are dependent on the compositional elements and experiments have shown that some high-entropy alloys exhibit an unusual increase in strength and ductility with decreasing temperature [44]. Others have also shown to have extraordinary mechanical properties in small samples and research suggests that some may have better resistance to radiation damage than conventional alloys [45, 46, 10].

Also one of the appealing aspects of developing high-entropy alloys is that because of the large compositional phase space the materials can be tuned for different main characteristics depending on the application to which they would be designed for [42, 9]. Alloys with one or two principal components typically have mechanical properties fairly similiar to the main constituent elements [41] whereas the multi-principal component alloys might have mechanical characteristics such as Young's modulus completely different from any of the composing elements [47].

Some of the suggested reasons for the varying mechanical properties of HEAs are the relatively high configurational entropy giving rise to stability of the single phase solid solution, lattice distortion and diffusion effects [9]. Some multi-principal component alloys exhibit sluggish diffusion and it has been introduced as a general characteristic of HEAs but recently it has been shown that the diffusion effects can be more versatile [37].

Due to the difficulties of having an accurate formal universal definition and, since many materials that do not fit to any of the given definions of HEA also possess a variety of the desired characteristics, authors often describe all of these under the same family of complex concetrated alloys (CCA) or multi-principal element alloys (MPEA) [37, 9].

3.2 Types of high-entropy alloys and their properties

The microstructure of the complex concentrated alloys depends on the constituent elements and, although CCAs in many different phases have been discovered, the vast majority contains BCC and FCC phase structures [41, 37]. Only certain mixtures of elements form solid solutions in multi-principal element alloys and for many applications the compositions need to be carefully chosen [41]. The general mechanical properties of HEAs also vary depending on their lattice structures: FCC high-entropy alloys tend to

be more ductile but have lower yield strength than BCC HEAs and some compositions contain both BCC and FCC structures simultaneously [48, 49, 41, 37].

Originally the study of high-entropy alloys was concentrated in the mixtures consisting mostly of principal elements from the so called Cantor alloy (CrMnFeCoNi), which was one of the earliest single phase solid-solutions found with multiple principal components [36]. This led to the research of HEAs formed from 3d transition metals (typically Co, Cr, Cu, Fe, Mn, Ni, Ti and/or V) and aluminum to study the effects of composition to the microstructure of the alloy and the whole field of research was mostly focused on these compounds. The 3d transition metal HEAs can be viewed as an extension for many familiar alloys such as stainless steels and nickel-based super alloys, which have a myriad of practical applications [9].

The lattice structure of the 3d transition metal CCAs without aluminum is typically FCC but can be adjusted from FCC to FCC + BCC and even to BCC by addition of Al to the mixture [34, 37]. Additions of other elements such as vanadium and molybdenum have also been studied in compositions similiar to Cantor alloy [35]. The final dominant phase is dependent on the Al concentration so that the microstructural preference goes rather continuously from FCC to BCC by increasing aluminum content. The most vastly researched types of HEAs are the mixtures based on Co, Cr and Ni with single-phase FCC microstructure [9, 37].

FCC HEAs are generally quite ductile and have an extraordinary property that both ductility and yield strength can increase with decreasing temperature [9]. A perhaps convenient property that research has shown FCC HEAs to possess is, that the strength of the formed alloy is generally a lot greater than the strength of the base elements by themselves. The strength to density ratio of the material can also be tuned by addition of certain elements such as V and Al [35]. Exceptional fracture toughness has also been reported among many of the FCC high-entropy alloys based on 3d transition metals some having even close to highest measured values of all materials. The measured toughness values range all the way from less than 1 to few hundred MPa$\sqrt{\text{m}}$ [50]. In transition metal based HEAs the fracture toughness can be seen to be closely related to the lattice structure of the alloy, single-phase FCC HEAs having the highest values and the value decreasing as the lattice structure advances towards more BCC concentrated structure [50]. Conversely hardness can be tuned by changing aluminum content in the mixture so that generally the hardness increases from FCC type HEAs to BCC type HEAs with increasing Al concentration [37].

Corrosion resistance is amongst the highly valued properties in many industrial applications and everyday use of materials, and HEAs have been shown to compete with many traditional corrosion-resistant materials [43]. In the earliest papers after the introduction of the term high-entropy alloys Chen et al. [51] compared the corrosion resistance

of $Cu_{0.5}$NiAlCoCrFeSi alloy and type-304 stainless steel (304S) in H_2SO_4 and NaCl solutions with varying concentrations, and showed that the HEA displayed lower corrosion rate in all solutions. The tested HEA was shown to also have a significantly higher hardness than the 304S but had a lower pitting potential in NaCl solutions. Lower pitting potential indicates a lower resistance to pitting corrosion, which is a form of corrosion that leads to formation of holes or pits in the substance [51]. Qiu et al. [52] studied electrochemical properties of many different high-entropy alloy compositions based on 3d transition metals in NaCl solution and their results show that many HEAs possess nobility in the range of austenitic stainless steel and pitting potential even higher than stainless steels.

Another type of high-entropy alloys, which has raised interest in the area of research, is the so called refractory HEAs (RHEA). Refractory HEAs usually consist of Mo, Nb, Ta, V and/or W as major elements but have been extended to include refractory elements Cr, Hf, Re, Zr, transition metals Co and Ni, and other elements such as Al, Ti, C, N and Si [53]. RHEAs typically seem to have BCC lattice structure and are often brittle at temperatures lower than room temperature [37], although for some mixtures the fracture toughness seem to be a lot higher for single crystal structrure than for bi-crystal [54]. Refractory HEAs have been shown have desired characteristics for many high temperature industrial applications. They often exhibit high strength and ductility at elevated temperatures as well as a high melting point [53]. Gorsse et al. [35] compared the properties of different high-entropy alloys from earlier experimental work to commercial alloys and showed that almost all refractory metal CCAs display significantly higher specific strength than commercially available refractory alloys.

Recently research in the field has shown promising properties of high-entropy alloys in terms of radiation resistance. Granberg et al. [10] used both experimental and computational methods to study the irradiation effects in Ni-based multicomponent alloys. In their work, Granberg et al. establish that the concentrated alloys have better radiation tolerance than elemental nickel and suggest that the mechanism for the resistance is associated with sluggish dislocation mobility, and support for this was later provided by computational means [55]. A different Ni-based multi-principal component alloy (FeNiMnCr) and its irradiation effects was researched by Kumar et al. [56]. They showed using experimental methods that the MPEA has significantly higher resistance to radiation damage compared to austenitic Fe-Cr-Ni alloys such as stainless steel. Similarly promising experimental results for nickel-based HEAs for the irradiation tolerance and structural stability has been shown in [57, 58, 11]. Recently El-Atwani et al. [12] revealed using experimental and computational methods some exceptional properties of tungsten-based BCC high-entropy alloys with respect to radiation resistance. The irradiation was done in room temperature and at a higher temperature (1073 K) both in

situ and ex situ and up to 8 dpa and no dislocation loops were observed and also only slight radiation-induced hardening was observed. Another refractory high-entropy alloy's tolerance against high-dosage radiation was investigated very recently by Chang et al. in [13]. They used 300 keV Ni^+ ions to irradiate HfNbTaTiZr samples up to 30 dpa and showed it to possess high overall resistance to irradiation. In one study [59] an abnormal radiation-induced phenomenon of $Ti_2ZrHfV_{0.5}Mo_{0.2}$ refractory HEA was observed, in which the lattice constant was shown to expand after high-dosage irradiation of He^+ ions. The examined RHEA suffered almost no hardening after the radiation treatment. Patel et al. [60] studied radiation tolerance of $V_{2.5}Cr_{1.2}WMoCo_{0.04}$ RHEA and showed yet again promising results of the as-cast BCC samples against high-dosage radiation. However their post-irradiation heat treatment (500h at 1460 K) gives evidence of metastability of the BCC phase, since three distinct phases was observed after the treatment. The authors note that this challenges the current understanding of the mechanisms behind the phase stability of some high-entropy alloys.

Clearly, high-entropy alloys have been shown to possess desirable qualities with respect to irradiation-induced damage tolerance. When compared to conventional materials typically used in environments exposed to high radiation, such as tungsten, some high-entropy alloys do not exhibit as much irradiation-induced embrittlement [12, 59]. Also in tungsten the defect mobilities are very dissimilar compared to the suggested similar values for defects in the refractory HEA investigated by El-Atwani et al. [12, 61].

Other types of complex concentrated alloys such as noble metal HEAs have also been under research but the most promising types for many industrial and energy production applications are the aforementioned transition metal HEAs and refractory HEAs. Possible applications for noble metal HEAs could be e.g. in industrial catalysts, and to make the HEAs more cost effective some commonly used 3d transition metals, such as Cu, Co, Cr and Ni, can also be added [9, 62].

The exceptional mechanical properties as well as corrosion and radiation resistance of high-entropy alloys with certain qualities spanning a wide range of values makes them a worthwhile research topic in the field of materials research. Specifically the encouraging results of irradiation tolerance of refractory HEAs gives hope for the development of materials for harsh environments of fusion reactors. Finding durable and economical materials for energy production applications could be a pivotal point determining a path to a more environmentally sustainable future.

4. Computational methods for materials research

4.1 General introduction

Alongside with experimental research, computational methods can be used to study the properties and structure of materials. Experimental results always contain sources of uncertainty and likewise, computational methods are based on different levels of approximations due to the extreme computational demands for solving the physical equations exactly. Different computational methods can vary from fully quantum mechanical calculations including the electronic structure explicitly to classical molecular dynamics simulations, where the interaction between individual atoms is described by approximated interatomic potentials (IAP) [63]. Deep understanding can be a great assistance in design and development of materials, but requires both experimentally characterized properties of materials and a theoretical framework for the observed qualities. Materials physics simulations can contribute to understanding the microscopic phenomena and characteristics displayed in experimental work and in many cases provide a bridge between experiments and theory.

4.1.1 Density Functional Theory

In ab initio methods the goal is to solve the non-relativistic Schrödinger equation for the whole simulated system including the electrons as well as the nuclei of the atoms. The hamiltonian for a system of M nuclei and N electrons becomes [64]:

$$\begin{aligned}\mathcal{H} = &-\sum_{i=1}^{N}\frac{\hbar^2}{2m_e}\nabla_i^2 - \sum_{j=1}^{M}\frac{\hbar^2}{2m_j}\nabla_j^2 + \frac{1}{2}\sum_{i=1}^{N}\sum_{i'\neq i}^{N}\frac{e^2}{4\pi\varepsilon_0|\boldsymbol{r}_i-\boldsymbol{r}_{i'}|} \\ &+\frac{1}{2}\sum_{j=1}^{M}\sum_{j'\neq j}^{M}\frac{Z_jZ_{j'}e^2}{4\pi\varepsilon_0|\boldsymbol{R}_j-\boldsymbol{R}_{j'}|} - \sum_{i=1}^{N}\sum_{j=1}^{M}\frac{Z_je^2}{4\pi\varepsilon_0|\boldsymbol{r}_i-\boldsymbol{R}_j|}\,,\end{aligned} \tag{4.1}$$

where $\boldsymbol{r}_i$ and $\boldsymbol{R}_j$ are the positions of electrons and nuclei respectively and Z_j and m_j are

the atomic number and mass of the nucleus j.

Since this task is computationally heavy even for small systems, approximations are done also in the ab initio methods such as the Born-Oppenheimer approximation, in which the motions of the electrons and the nuclei can be considered separately and therefore also the wavefunction of the system becomes separable. Different ab initio methods include Hartree-Fock, Post-Hartree-Fock, Multi-reference methods and also Density functional theory (DFT), which is one of the most popular methods in computational chemistry and condensed matter physics [65].

The origins of the Density functional theory lie in the Thomas-Fermi model, where the ground state energies of atomic systems are calculated as an approximated functional of electron density and this is the key idea also behind modern DFT: instead of solving for the many-body wavefunction of the electrons, find the electron density and study the system's properties as functionals of this density [65]. Pierre Hohenberg and Walter Kohn layed the foundation for the current DFT by providing rigorous proofs to two vital theorems, now called Hohenberg-Kohn theorems, which state that [66]:

- *The external potential is a unique functional of the electron density of the system*
- *The functional, that gives the ground-state energy of the system, attains the minimum value with respect to possible electron densities if and only if the input density is the true ground-state density.*

From the first theorem it also follows that the properties defined by the external potential are uniquely determined by the ground-state density. In Density functional theory the Born-Oppenheimer approximation is assumed as is usual in multi-atom quantum mechanical computations [65].

The problem would still be intractable due to the interaction between the electrons and the inaccuracy in the kinetic energy term until W. Kohn and L. J. Sham introduced a method to overcome this issue: instead of solving the system of interacting electrons, replace the system with non-interacting particles moving in a fictitious effective potential so that the density of the particles remains the same [67]. The equations (called Kohn-Sham equations) describing this fictitious system are

$$\Big(-\frac{\hbar^2}{2m_i}\nabla^2 + v_{\text{eff}}(\boldsymbol{r})\Big)\psi_i(\boldsymbol{r}) = \varepsilon_i\psi_i(\boldsymbol{r}) \tag{4.2}$$

$$n(\boldsymbol{r}) = \sum_{i=1}^{N} |\psi_i(\boldsymbol{r})|^2 \ , \tag{4.3}$$

where ε_i is the orbital energy of the so called Kohn-Sham orbital ψ_i and n is the density of the N-particle system. The energy functional becomes

$$E[n(\boldsymbol{r})] = T[n(\boldsymbol{r})] + \frac{1}{2}\int\int \frac{n(\boldsymbol{r})n(\boldsymbol{r}')}{4\pi\varepsilon_0|\boldsymbol{r}-\boldsymbol{r}'|}\mathrm{d}\boldsymbol{r}\mathrm{d}\boldsymbol{r}' + \int v_{\text{ext}}(\boldsymbol{r})n(\boldsymbol{r})\mathrm{d}\boldsymbol{r} + E_{\text{xc}}[n(\boldsymbol{r})] \ , \tag{4.4}$$

where $T[n(\boldsymbol{r})]$ is the kinetic energy of the system of non-interacting particles, the second term is the electronic coulomb energy, v_{ext} is the external coulomb potential caused by the nuclei and E_{xc} is the exchange-correlation functional. Unfortunately the exact form of the exchange-correlation functional is unknown, but a large number of approximate functionals has been developed over the past decades. The electron density and the ground state energies are calculated by iteratively solving the Kohn-Sham equations. First an initial guess for the electron density is given, then the effective potential is computed and again the electron density from the obtained potential. This cycle is repeated until the system is self-consistent [65].

As in all ab initio methods the orbitals are represented as a sum of certain basis functions also in DFT. The VASP-software [68] used in this thesis work uses plane-wave basis sets:

$$\psi_{m,\boldsymbol{k}}(\boldsymbol{r}) = \sum_{\boldsymbol{G}}^{|\boldsymbol{G}|<G_{\max}} c_{m,(\boldsymbol{k}+\boldsymbol{G})}\ e^{i(\boldsymbol{k}+\boldsymbol{G})\cdot\boldsymbol{r}}\ , \tag{4.5}$$

where $\psi_{m,\boldsymbol{k}}$ is the component of the wave function of an electron at band m, $\boldsymbol{k}$ is the wave vector and $\boldsymbol{G}$ are reciprocal lattice vectors. Since the basis set is infinite in terms of vectors $\boldsymbol{G}$, a cutoff value $G_{\max}$ is used. The plane-wave basis has a lot of advantages, but requires a method to simplify the orbitals near the atom cores due to the rapid oscillations of the wavefunctions. This is achieved by using pseudopotentials at the core region so that the wavefunctions outside this region remain the same and therefore also the dynamics of the system, since the chemical bonding involves almost exclusively valence electrons [69, 68].

4.1.2 Classical Molecular Dynamics

Because of the high computational demands of quantum mechanical calculations, a more efficient method, classical Molecular Dynamics (MD), is often used in materials simulations. Though a less accurate method, Molecular Dynamics simulations can be used to study much larger systems with longer simulation times and is therefore a valuable tool in materials research. The accuracy of MD relies heavily on the quality of the interatomic potentials describing the atomic interactions [70].

In classical Molecular Dynamics simulations, the atoms and molecules of the system are treated as classical particles interacting via artificial interactions and their motion is studied by numerically solving Newton's equations of motion [14]:

$$m_i \frac{\mathrm{d}^2\boldsymbol{r}_i}{\mathrm{d}t^2} = \boldsymbol{f}_i \tag{4.6}$$

$$\boldsymbol{f}_i = -\nabla_i V\ , \tag{4.7}$$

where $\boldsymbol{r}_i$, m_i and $\boldsymbol{f}_i$ are the position, mass and force acting on particle i respectively and

V is the potential energy. Again the Born-Oppenheimer approximation is assumed and the electrons are taken to be in eigenstates the motion of the nuclei is considered under the potential. Also the bonds between individual atoms are included in the interatomic potential. The integration of the equations of motion is done by adding small increments to positions and velocities depending on the forces acting on the particles and therefore timestep is an important parameter: the value should be small enough for sufficient accuracy but not at the expense of efficiency. Although it would be possible to integrate Newton's equations of motion using the simple Euler algorithm, more sophisticated methods have been developed, which provide more accurate calculations with less computation time and memory usage and allow for larger timestep values, such as the Velocity Verlet algorithm and Predictor-Corrector algorithms [14]. A schematic image of the complete MD simulation algorithm is shown in Figure 4.1.

For many interatomic potentials used in MD, it is unnecessary to compute all interactions between every particle with every step because only the interactions between nearby particles have a noticeable effect. Therefore a cut-off distance is often determined and the interactions are limited within the range of that cut-off value. Also since even the smallest experimental systems usually contain much more atoms than what would be plausible to simulate, periodic boundary conditions can be used in the simulation cell to effectively model larger systems [14].

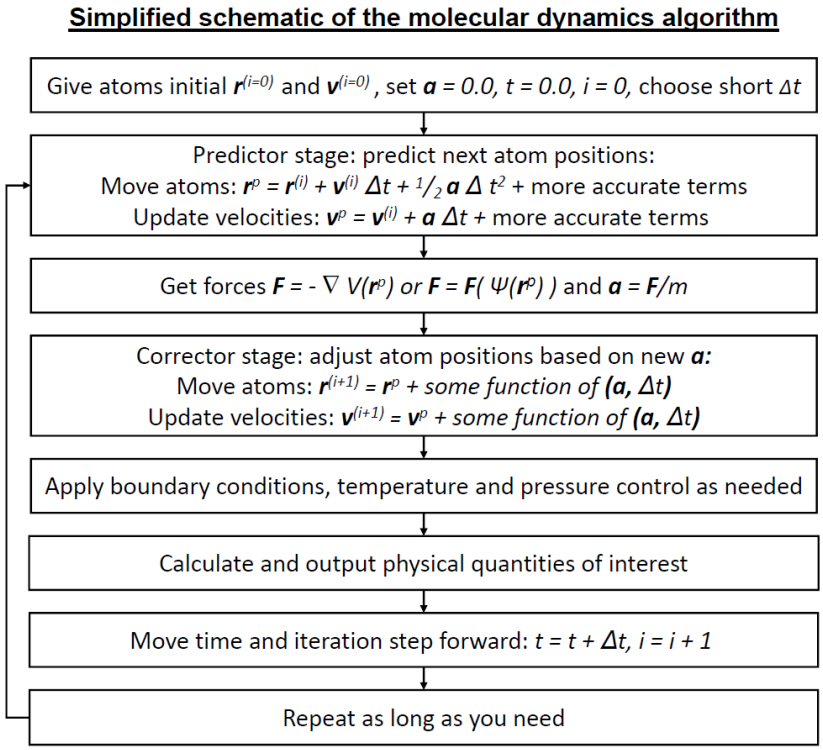

Figure 4.1: Molecular Dynamics simulations algorithm. Image source: [71]

Typically one wants to analyze the macroscopic properties of the simulated system and compare the results to experimental research. Therefore MD simulations are often conducted so that the ergodic hypothesis holds and macroscopic properties can be studied by obtaining time averages from the simulation. Also since experiments are usually done in a controlled environment such as constant temperature and pressure, these thermodynamic properties of the system must be controlled in a manner, which prevents too many artefacts arising in the simulations. This is done by adjusting the dynamics so that the simulation represents the correct thermodynamic process. Different thermostats and barostats have been developed for this purpose such as Berendsen and Nosé-Hoover thermostats for temperature control and Andersen and Parrinello-Rahman barostats for pressure control [14].

4.2 Interatomic potentials

4.2.1 History

The accuracy and efficiency of MD is largely dependent on the interatomic potential, which therefore plays a crucial role in the usefulness of the simulations [15]. The development of Molecular Dynamics can be seen to begin in the 1950s although many of the methods used in modern MD were already developed much earlier [14]. At the time the available computational power was obviously a lot less sufficient so the first interatomic potentials had to have a particularly simple form.

The earliest potentials were pair potentials approximating the potential energy as a function of distance between two particles. The first ones were extremely simple such as the hard and soft sphere potentials and the square well potential [14]. To develop pair potentials further, both short range repulsive part and the attractive part needed to be taken in consideration. The repulsive interaction at small interatomic distances originates from the coulombic interaction of charged particles of same sign and the Pauli exclusion principle. The attractive part also has its origin in the coulombic interaction, which causes binding of atoms by different mechanisms [65]. One of the earliest and well-know potentials is the Lennard-Jones potential, published in 1924, with the potential energy function [72]:

$$V_{\mathrm{LJ}}(r) = 4\varepsilon\left[\left(\frac{\sigma}{r}\right)^{12} - \left(\frac{\sigma}{r}\right)^{6}\right], \tag{4.8}$$

where r is the interatomic distance and σ and ε are parameters of the model to be determined either by experiments or more accurate calculations. While having a crude form the Lennard-Jones potential can be fairly successful in simulating weakly interacting particles such as noble gases [14]. Figure 4.2 shows the Lennard-Jones potential as a function of r and contributions of the repulsive and attractive parts.

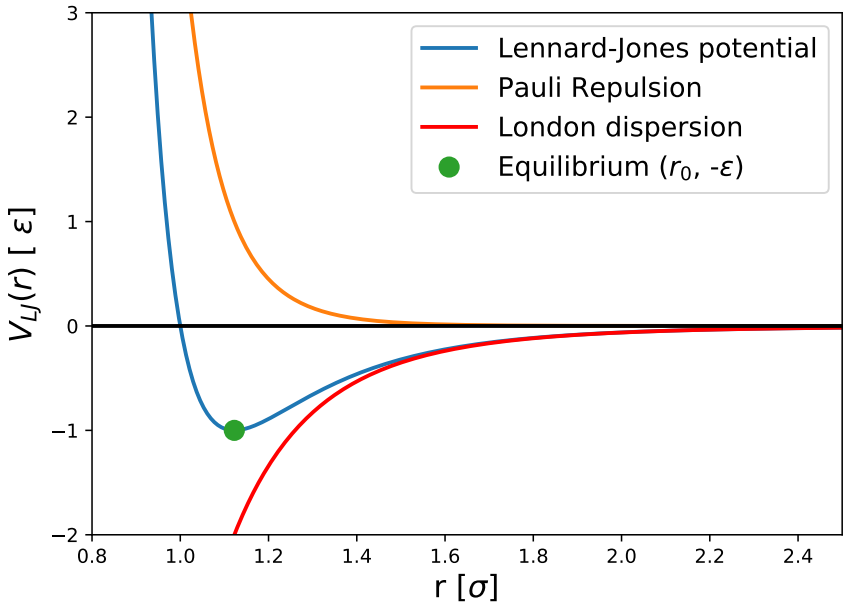

Figure 4.2: Illustration of the Lennard-Jones potential. r_0 is the distance at the minimum of the potential.

Although the Lennard-Jones potential gives a decent model for inert gases near equilibrium conditions, it fails severely at close interatomic distances due to the too slow growth of the repulsive part when $r \to 0$. Some extensions have been developed to the Lennard-Jones potential since its publication such as the Buckingham potential, which has a more physically justifiable exponential function as the repulsive term [73]:

$$V_{\text{Buck}}(r) = Ae^{-Br} - \frac{C}{r^6} \ . \tag{4.9}$$

A few years after the Lennard-Jones potential in 1929, Philip M. Morse published his interatomic potential model mainly for diatomic molecules and showed that analytical solutions for the Schrödinger equation with this potential exist [74]. In the so called Morse potential the potential energy is

$$V_{\text{M}}(r) = D_e(1 - e^{-a(r-r_e)})^2 \ , \tag{4.10}$$

where r_e and D_e are the equilibrium distance of the atoms and depth of the potential energy well at equilibrium respectively. The Morse potential gives a better description of diatomic vibrations than the harmonic oscillator potential, since it produces more physical effects such as anharmonicity [74].

For the potentials to properly describe systems far from the equilibrium conditions such as radiation effects, where the interatomic distances can be extremely small, the repulsive part of the potential needs to be handled with care. Since the repulsion at really

short distances is mainly due to the Coulombic interaction between the nuclei, different screened Coulombic potentials were developed to model the interatomic repulsion. A successful and much used model for the repulsive part was created by Ziegler, Biersack and Littmark [75] and has the form:

$$V_{\mathrm{ZBL}}(r) = \frac{1}{4\pi\varepsilon_0}\frac{Z_i Z_j e^2}{r}\phi\Big(\frac{r}{a}\Big) \ , \tag{4.11}$$

$$a = \frac{0.8854 a_0}{Z_i^{0.23} + Z_j^{0.23}} \ , \tag{4.12}$$

where Z_i is the atomic number of atom i and $\phi(r/a)$ is a universal screening function

$$\phi(x) = 0.1818e^{-3.2x} + 0.5099e^{-0.9423x} + 0.2802e^{-0.4028x} + 0.02817e^{-0.2016x} \tag{4.13}$$

and a_0 is the Bohr radius.

4.2.2 Overview of potentials

Though many of the earliest interatomic potentials were pair potentials, they all suffer from serious limitations in describing physical properties of most materials realistically. This is due to the fact that it is virtually impossible to take in to account the environmental effects to the atomic interactions by using only pair interactions [14]. Hence the modern potentials used are many-body potentials, that can in general be written as a sum of many-body and single-body terms:

$$V_{\text{many-body}} = \sum_i V_1(\boldsymbol{r}_i) + \frac{1}{2}\sum_{ij} V_2(\boldsymbol{r}_i, \boldsymbol{r}_j) + \frac{1}{3!}\sum_{ijk} V_3(\boldsymbol{r}_i, \boldsymbol{r}_j, \boldsymbol{r}_k) + ... \tag{4.14}$$

and the V_1 term is usually omitted, since it accounts for some external potential which the system interacts with.

A groundwork for many of the potentials used today especially for metals, was layed when a method based on density functional theory was introduced; In this so called Effective-medium theory (EMT) the material is represented by a homogeneus electron gas with a static positive background density in which added impurities interact [76, 77]. The modern well-known Embedded atom method (EAM), originally developed by Daw and Baskes [78], has roots in EMT and has a similar expression for the potential energy at atom i:

$$V_i^{\mathrm{EAM}} = F_i(\rho_i) + \frac{1}{2}\sum_j \phi_{ij}(r_{ij}) \ , \tag{4.15}$$

where ϕ is the repulsive pair potential often in the form of screened Coulomb potential and r_{ij} is the distance between atoms i and j. F_i is the embedding function representing

the energy of embedding an atom to the system and depends on the total electron density at atom i

$$\rho_i = \sum_{j \neq i} \rho_j^a(r_{ij}) \ , \tag{4.16}$$

where ρ^a is electron density of atom j. The form of the embedding function, atomic electron density and the repulsive potential can be deduced by using ab initio methods and fitting to experimental results [79]. Many EAM-like potentials have been developed in the past decades and also, since the original EAM formulation does not take into account the angular dependence of the atoms' positions, modified versions have been introduced to include directional dependence in the electron density [80].

An interatomic potential with explicit angular dependence developed for silicon was introduced by Stillinger and Weber in 1985 [81] and the potential energy can be expressed as

$$V_{\mathrm{SW}} = \sum_{i<j} V_2(r_{ij}) + \sum_{\substack{i \neq j,k \\ j<k}} V_3(r_{ij}, r_{ik}, \theta_{ijk}) \ . \tag{4.17}$$

The pair and three-body parts V_2 and V_3 are

$$V_2(r_{ij}) = \Big(A_{ij} r_{ij}^{-p_{ij}} - B_{ij} r^{-q_{ij}}\Big) \exp\Big[(r_{ij}/\sigma_{ij} - a_{ij})^{-1}\Big] \tag{4.18}$$

$$V_3(r_{ij}, r_{ik}, \theta_{ijk}) = \lambda_{ijk} \exp\left(\frac{\gamma_{ij}}{r_{ij}/\sigma_{ij} - a_{ij}^2} + \frac{\gamma_{ik}}{r_{ik}/\sigma_{ik} - a_{ik}^2}\right)\Big(\cos(\theta_{ijk}) + \frac{1}{3}\Big) \ , \tag{4.19}$$

where θ_{ijk} is the angle between atom bonds ij and ik and $A, B, p, q, \sigma, \lambda$ and γ are parameters of the model and a is the cutoff radius: $V_n = 0$ if $r_{ij}/\sigma_{ij} >= a_{ij}$ for $n = 1, 2$ and for any summed indices i, j. The Stillinger-Weber potential provides fairly good results for both crystalline and liquid silicon [81].

A problem with this type of explicit angular-dependent potentials is that though they may do well with certain materials, they fail to represent systems with differing atomic structures. Another way of describing environmental effects to the system's potential energy is to use the concept of bond-order, so that the strength of the atomic bonds is taken in to account, as the strength typically decreases with increasing number of bonds [82, 83]. Generally bond-order potential can be expressed as

$$V_{\mathrm{BOP}} = V_{\mathrm{repulsive}}(r_{ij}) + b_{ijk} V_{\mathrm{attractive}}(r_{ij}) \ , \tag{4.20}$$

where b_{ijk} is a function depending on the number of neighbours; usually a monotonically decreasing function of the bond-order. A forerunner for many modern bond-order potentials was developed by J. Tersoff [83], which had the atomic potential energy in form

$$V_{\mathrm{Tersoff}} = f_{\mathrm{C}}\Big(a_{ij} f_{\mathrm{R}}(r_{ij}) + b_{ij} f_{\mathrm{A}}(r_{ij})\Big) \ , \tag{4.21}$$

where f_{R} and f_{A} are the repulsive and attractive terms respectively and f_{C} is a cutoff function for the potential. The repulsive and attractive terms are

$$f_{\mathrm{R}}(r) = Ae^{-\lambda_1 r} \tag{4.22}$$

$$f_{\mathrm{A}}(r) = -Be^{-\lambda_2 r} \ . \tag{4.23}$$

The cutoff term f_{C} is a monotonically decreasing function of r and has values from 1 to 0 with a smooth transition within a chosen transition width. The function a_{ij} contains only terms related to limiting the range, but is often neglected completely by making an approximation so that $a_{ij} \approx 1$. The term b_{ij} however is the important part containing the essential parameters for taking into account the contributions of the coordination numbers and angles of the bonds [83], and has the form:

$$b_{ij} = \left(1 + \beta^n \zeta_{ij}^n\right)^{-1/2n} \tag{4.24}$$

$$\zeta_{ij} = \sum_{k \neq i,j} f_C(r_{ij}) g(\theta_{ijk}) \ e^{\lambda_3^3 \ (r_{ij} - r_{ik})^3} \tag{4.25}$$

$$g(\theta) = 1 + \frac{c^2}{d^2} - \frac{c^2}{d^2 + (h - \cos\,\theta)^2} \ , \tag{4.26}$$

where θ_{ijk} is the angle between bonds ij and ik

Interatomic potentials are typically developed for predicting equilibrium properties and hence can fail when the system is far from equilibrium. Therefore a separate repulsive part is often used and careful joining of the repulsive part with the used IAP is extremely important. Many other potentials, that are not reviewed in this thesis, have been developed over the past decades. Some important ones to mention are the molecular force fields and the ReaxFF [84], that allows for the formation and breaking of chemical bonds, and bond-order potentials employing the tight-binding theory [85, 86].

The conventional interatomic potentials having a fixed functional form suffer from inherently limited capability in describing complicated phenomena due to the inflexibility of the potentials. In order to make the IAPs able to describe many properties of materials and physical phenomena accurately, a large number of fitting parameters are needed and the functional forms become increasingly complex. This has led to the development of machine learning potentials, which have no restrictions in the required flexibility. The development of machine learning IAPs began already in the 1990s but they started drawing general attention only after Behler and Parrinello published their work on neural-network potentials [87]. Another type of machine learning potential, originally developed by Bártok et al. [88, 16], is based on Gaussian process regression: The Gaussian approximation potential (GAP). Recently it has been shown to be able to produce accurate potentials for transition metals [89]. Other types of machine learning IAPs have also been created employing many other non-parametric and machine learning methods, and even more is

currently under development. Machine learning may provide methods to develop more flexible and accurate potentials but are heavily dependent on the quality of the training data.

4.2.3 Gaussian Approximation Potentials

Gaussian process regression

The theoretical framework behind the Gaussian Approximation Potentials is Gaussian process regression (GPR), which is a non-parametric regression method. In parametric approaches the response variable $y(\boldsymbol{x})$ is usually modeled as a linear combination of some generally nonlinear basis functions $\{\varphi_h(\boldsymbol{x})\}_{h=1}^{H}$ parameterized by the parameter vector $\boldsymbol{w}$:

$$y(\boldsymbol{x};\boldsymbol{w}) = \sum_{h=1}^{H} w_h \varphi_h(\boldsymbol{x}), \tag{4.27}$$

where $\boldsymbol{x}$ is the input vector. In the Bayesian framework, the distribution over the parameters $\boldsymbol{w}$ can then be infered by setting a prior probability distribution $P(\boldsymbol{w})$ and using Bayesian inference to obtain the posterior distribution:

$$P(\boldsymbol{w}|y,\boldsymbol{x}) = \frac{P(y|\boldsymbol{w},\boldsymbol{x})P(\boldsymbol{w})}{P(y|\boldsymbol{x})}. \tag{4.28}$$

For making predictions the predictive posterior distribution can then be computed by marginalizing over the sampling distribution over the posterior probability of the parameters. In Gaussian process regression however, instead of directly parameterizing the response variable $y(\boldsymbol{x})$ and modeling the distribution over the parameters, the distribution over all the possible functions is modeled [90, 91].

A Gaussian process can be defined as a continuous stochastic process $y : X \to \mathbb{R}$ for which every finite subset $X_N = \{\boldsymbol{x}_1, ..., \boldsymbol{x}_N\}$, the joint distribution $P(\boldsymbol{y}) = P(y(\boldsymbol{x}_1), \ldots, y(\boldsymbol{x}_N))$ is a multivariate normal distribution. Just as the Gaussian distribution is completely determined by its mean and covariance matrix, the Gaussian process is completely determined by its mean and covariance function [90]. If the prior for the weights in (4.27) is set to be a Gaussian distribution with zero mean $P(\boldsymbol{w}) = \mathcal{N}(\boldsymbol{w}; \boldsymbol{0}, \sigma_w \boldsymbol{I})$ then $y(\boldsymbol{x};\boldsymbol{w})$ is a Gaussian process, since it is a linear in the parameters $\boldsymbol{w}$. The covariance function is then

$$k(\boldsymbol{x},\boldsymbol{x'}) = \mathbb{E}[y(\boldsymbol{x})y(\boldsymbol{x'})] = \Big\langle \sum_{hh'} w_h w_{h'}\ \varphi_h(\boldsymbol{x})\varphi_{h'}(\boldsymbol{x'}) \Big\rangle \tag{4.29}$$

$$= \sum_{hh'} \langle w_h w_{h'} \rangle \varphi_h(\boldsymbol{x})\varphi_{h'}(\boldsymbol{x'}) = \sigma_w \sum_h \varphi_h(\boldsymbol{x})\varphi_h(\boldsymbol{x'}) \tag{4.30}$$

since $\langle w_h w_{h'} \rangle = \delta_{h,h'}\sigma_w$. If we consider N target values $\boldsymbol{t}_N = \{t_n\}_{n=1}^{N}$ for N input vectors $\{\boldsymbol{x}_n\}_{n=1}^{N}$ and the measured target value t_n is assumed to contain some additional Gaussian

distributed noise with variance σ_ν^2, the covariance matrix for target vector $\boldsymbol{t}_N$ becomes

$$\mathbf{C}_N = \mathbf{Q} + \sigma_\nu^2 \mathbf{I}, \tag{4.31}$$

where the elements of $\mathbf{Q}$ are

$$Q_{pq} = k(\boldsymbol{x}_p, \boldsymbol{x}_q) = \sigma_w \sum_h \varphi_h(\boldsymbol{x}_p)\varphi_h(\boldsymbol{x}_q) \tag{4.32}$$

and the target vector has a prior distribution $P(\boldsymbol{t}_N) = \mathcal{N}(\boldsymbol{t}_N; \mathbf{0}, \mathbf{C}_N)$ [90].

Predictions for new target value t_{N+1} can then be made by noting that, since $P(\boldsymbol{t}_N)$ is a Gaussian distribution then also the joint probability distribution $P(t_{N+1}, \boldsymbol{t}_N)$ is a Gaussian. Now the posterior predictive distribution is

$$P(t_{N+1}|\boldsymbol{t}_N) = \frac{P(t_{N+1}, \boldsymbol{t}_N)}{P(\boldsymbol{t}_N)} \propto \exp\Big(-\frac{1}{2}\boldsymbol{t}_{N+1}^{\mathrm{T}} \mathbf{C}_{N+1}^{-1} \boldsymbol{t}_{N+1}\Big), \tag{4.33}$$

where $\boldsymbol{t}_{N+1}^{\mathrm{T}}$ is the vector $[\boldsymbol{t}_N \;\; t_{N+1}]$ and $\mathbf{C}_{N+1}$ is the covariance matrix with submatrices

$$\mathbf{C}_{N+1} = \begin{bmatrix} \mathbf{C}_N & \boldsymbol{k} \\ \boldsymbol{k}^{\mathrm{T}} & k_{N+1} \end{bmatrix}, \tag{4.34}$$

where $\boldsymbol{k}$ is the vector containing all the covariances between the original N targets and the new $(N+1)$:th target: $\boldsymbol{k}^{\mathrm{T}} = [\, k(\boldsymbol{x}_1, \boldsymbol{x}_{N+1}), \ldots, k(\boldsymbol{x}_N, \boldsymbol{x}_{N+1}) \,]$. Instead of directly inverting the $\mathbf{C}_{N+1}$ matrix, it can be shown that the inverse can be written as [91]

$$\mathbf{C}_{N+1}^{-1} = \begin{bmatrix} \mathbf{M} & \boldsymbol{m} \\ \boldsymbol{m}^{\mathrm{T}} & m \end{bmatrix}, \tag{4.35}$$

where

$$m = (k_{N+1} - \boldsymbol{k}^{\mathrm{T}} \mathbf{C}_N^{-1} \boldsymbol{k})^{-1} \tag{4.36}$$

$$\boldsymbol{m} = -m \mathbf{C}_N^{-1} \boldsymbol{k} \tag{4.37}$$

$$\mathbf{M} = \mathbf{C}_N^{-1} + \frac{1}{m} \boldsymbol{m}\boldsymbol{m}^{\mathrm{T}} \tag{4.38}$$

and now the posterior predictive distribution becomes

$$P(t_{N+1}|\boldsymbol{t}_N) \propto \exp\Big(-\frac{(t_{N+1} - \hat{t}_{N+1})^2}{2\sigma_{\hat{t}_{N+1}}^2} \Big) \tag{4.39}$$

with

$$\hat{t}_{N+1} = \boldsymbol{k}^{\mathrm{T}} \mathbf{C}_N^{-1} \boldsymbol{t}_N \tag{4.40}$$

$$\sigma_{\hat{t}_{N+1}}^2 = k_{N+1} - \boldsymbol{k}^{\mathrm{T}} \mathbf{C}_N^{-1} \boldsymbol{k} \; . \tag{4.41}$$

The predicted target value for the new data point is taken as the mean of this distribution, which can easily be seen to be $\hat{t}_{N+1}$ and which is also the maximum a posteriori (MAP) estimate, and $\sigma_{\hat{t}_{N+1}}$ gives the standard deviation for the prediction. The above derivation follows closely the example shown in [91].

The predicted value can also be written as

$$\hat{t}_{N+1} = \sum_{n=1}^{N} \alpha_n k(\boldsymbol{x}_n, \boldsymbol{x}_{N+1}) \tag{4.42}$$

where the coefficients are defined as

$$\{\alpha_n\} = \boldsymbol{\alpha} = \mathbf{C}_N^{-1} \boldsymbol{t}_N \ . \tag{4.43}$$

From this it becomes obvious, that the parameters and the basis functions are never required explicitly, but only the covariance function needs to be defined.

Covariance functions

The covariance function determines the gaussian process and can be viewed as a measure of similarity between the points. The only restriction for a covariance function to be valid is that it is a positive-definite kernel i.e. a function $K : X \times X \to \mathbb{R}$ for which

$$\sum_{i=1}^{n} \sum_{j=1}^{n} w_i w_j K(x_i, x_j) \geq 0 \tag{4.44}$$

for any $\{x_i \in X\}_{i=1}^n$ and $\{w_i \in \mathbb{R}\}_{i=1}^n$. It can be shown that for every positive definite function there exists a corresponding expansion in some basis with possibly infinite nonlinear basis functions. This is at the heart of the usefulness of GPR: for making predictions, only the covariance function, or the kernel, needs to be defined, but the similarity is taken in a higher dimentional space even though no transformation is explicitly conducted [90].

A covariance function is said to be stationary if it is a function of only $\boldsymbol{x} - \boldsymbol{x'}$ and is therefore invariant to translations. Similarly, isotropic covariance function is a function of $|\boldsymbol{x} - \boldsymbol{x'}|$ and hence is invariant also to rotations. Dot product covariance functions are functions of only the dot products of the points $\boldsymbol{x}^{\mathrm{T}}\boldsymbol{x'}$ or generally $\boldsymbol{x}^{\mathrm{T}}\Sigma_p\boldsymbol{x'}$ with a covariance matrix Σ_p. A common covariance function is e.g. the generalized squared exponential kernel

$$K(\boldsymbol{x}_p, \boldsymbol{x}_q) = \sigma_f^2 \exp\Big(-\frac{1}{2l^2}|\boldsymbol{x}_p - \boldsymbol{x}_q|^2 \Big) + \delta_{pq}\sigma_n^2 \ , \tag{4.45}$$

where σ_f, σ_n and l are the hyperparameters of the model. Another much used kernel function is the polynomial kernel

$$K(\boldsymbol{x}, \boldsymbol{x'}) = \delta^2(\boldsymbol{x}^{\mathrm{T}}\Sigma_p\boldsymbol{x'} + \sigma_0^2)^p \ , \tag{4.46}$$

with a positive integer p, hyperparameters σ_0 and δ and covariance matrix Σ_p. The choice of hyperparameters of the covariance function alters the behavior of the gaussian process model and should therefore be treated with care. Optimization methods for the hyperparameters exist but they can also be reasoned by using prior knowledge of the subject [90, 91].

Descriptors

Now, since the objective is to describe potential energies for atoms in a system, the input data points need to represent the atomic environments. Also for the potential to be efficient in use, the input points need to be obtained as easily as possible, and this has turned out to be a challenging task. The data points used in machine learning potentials are so called descriptors, which are functions of the positions of neighbouring atoms within some cutoff radius and effectively give a mathematical description of the atom's environment [16, 92]. Since the energies of atoms and forces acting on them can not depend on the location or orientation in space, but only on the surrounding environment, the descriptors are restricted to being invariant under rigid transformations. Also permutations of identical particles should not have an effect on the system [92]

Many descriptors satisfying the conditions have been introduced and the most simple is the two-body descriptor, which is the euclidean distance between two atoms: $q = |\boldsymbol{r} - \boldsymbol{r'}|$, where $\boldsymbol{r}$ and $\boldsymbol{r'}$ are positions of atoms. Another possible option is the three-body descriptor with symmetrized triplets of interatomic distances: $\boldsymbol{q} = [r_{ik} + r_{ij}, (r_{ik} - r_{ij})^2, r_{jk}]^{\mathrm{T}}$, where r_{ij} is the distance between atoms i and j [88]. A commonly used descriptor with GAP is the smooth overlap of atomic positions (SOAP) descriptor, in which the local environment of an atom is given by the densities of neighbouring atoms' positions. Similarity is measured by integrating the overlap of the two environments [92]. In SOAP the atomic densities are described by setting a gaussian function centered at the atom's position so that the overlap is smoothened instead of having only pointlike densities:

$$\rho_i(\boldsymbol{r}) = \sum_j \exp\left(- \frac{|\boldsymbol{r} - \boldsymbol{r}_{ij}|^2}{2\sigma^2_{\mathrm{atom}}} \right) f_{\mathrm{cut}}(r_{ij}) \ . \tag{4.47}$$

The integration or the dot product between the SOAP descriptors gives the covariance function and is made rotationally invariant by integrating over all possible rotations [92]:

$$K(\rho_i, \rho_j) = \int \mathrm{d}\hat{R} \left| \int \rho_i(\boldsymbol{r}) \rho_j(\hat{R}\boldsymbol{r}) \right|^{\zeta} \ . \tag{4.48}$$

In practice the SOAP descriptor is implemented as an expansion of radial basis functions $\{g_n(r)\}$ and spherical harmonics $Y_{nlm}(\boldsymbol{r})$. For atom i this becomes:

$$\rho_i(\boldsymbol{r}) = \sum_{nlm} c^{(i)}_{nlm} \ g_n(r) Y_{nlm}(\hat{\boldsymbol{r}}) \tag{4.49}$$

from which the power spectrum elements are computed:

$$p^{(i)}_{nn'l} = \frac{1}{\sqrt{2l+1}} \sum_m c^{(i)}_{nlm} (c^{(i)}_{n'lm})^* \tag{4.50}$$

and the covariance in rotationally invariant form for atoms i and j is after normalization:

$$K'(\rho_i, \rho_j) = |\hat{\boldsymbol{p}}_i^{\mathrm{T}} \hat{\boldsymbol{p}}_j|^\zeta = \frac{|\boldsymbol{p}_i^{\mathrm{T}} \boldsymbol{p}_j|^\zeta}{|\boldsymbol{p}_i||\boldsymbol{p}_j|} \ , \tag{4.51}$$

where $\boldsymbol{p}_i$ is a vector of all components from $\{p^{(i)}_{nn'l}\}$ [92, 88, 93]. Also a hyperparameter δ is added to determine the energy scale of the SOAP kernel:

$$K'(\rho_i, \rho_j) = \delta^2 |\hat{\boldsymbol{p}}_i^{\mathrm{T}} \hat{\boldsymbol{p}}_j|^\zeta \ . \tag{4.52}$$

Data set accuracy and short range interactions

Since the gaussian approximation potentials contain no theoretical background from physics but relies only on the results given from the training data set, it is crucial to have enough accurate data points to produce a good quality potential. The training data set should be typically built with ab initio methods, such as DFT for instance, to ensure the accuracy of the fitting data. Also as for the conventional interatomic potentials it is necessary to carefully fit GAP to a separate repulsive potential (e.g. ZBL [75]), which should accurately describe the atomic interactions at very short distance. Proper fitting can be ensured by adding enough data points within the medium range region between the extremely short distances and longer distances.

In order for the GAP to be actually feasible to train and use, a sparsification algorithm needs to be applied to the training data set. The computational loads for training the GPR model and making predictions scale as $O(N^3)$ and $O(N)$ respectively with N training data points, but can be reduced to scale as $O(NM^2)$ and $O(M)$ by using only M sparse points [94]. This can be justified since the atomic environments in the training data are often redundant and very close to each other with respect to the similarity measure. Therefore to make a useful potential it is more efficient to retain only sparse data points. After the sparsification the solution for the coefficients in (4.42) becomes [93]:

$$\boldsymbol{\alpha}_s = [\mathbf{K}_{MM} + (\mathbf{L}\mathbf{K}_{NM})^{\mathrm{T}} \boldsymbol{\Lambda}^{-1} \mathbf{L}\mathbf{K}_{NM}]^{-1} (\mathbf{L}\mathbf{K}_{NM})^{\mathrm{T}} \boldsymbol{\Lambda}^{-1} \boldsymbol{y}_N \ , \tag{4.53}$$

where $\mathbf{K}$ is the kernel matrix with N total and M sparse training data environments, $\Lambda = \sigma_\nu^2 \mathbf{I}$ represents the errors in the training data and $\boldsymbol{y}$ contains total energies, forces and stress components of the whole training data. $\mathbf{L}$ is a linear operator for which $\mathbf{L}\boldsymbol{y}' = \boldsymbol{y}$, where $\boldsymbol{y}'$ contains the atomic energies instead of total energies [93].

Simulating atoms with GAP

When training a GAP, multiple types of descriptors and coviariance functions can be used [88]. The energies of atomic configurations predicted by GAP can then be computed for atom i as in (4.42):

$$E_i = \sum_d \sum_m^M \alpha_{m,d} K_d(\boldsymbol{q}_{i,d}, \boldsymbol{q}_{m,d}) \ , \tag{4.54}$$

where M is the number of sparse input points and d notes the different types of descriptors. The total potential energy of the system with external repulsive potential now becomes [88]:

$$E_{\text{total}} = \sum_{i<j} V_{\text{rep}}(r_{ij}) + \sum_d \sum_i^N \sum_m^M \alpha_{m,d} K_d(\boldsymbol{q}_{i,d}, \boldsymbol{q}_{m,d}) \ , \tag{4.55}$$

where N is the total number descriptors for each type and V_{rep} is the repulsive pair potential. The force acting on atom i is related to total energy via

$$f_{i\alpha} = \frac{\partial E}{\partial r_{i\alpha}} = \sum_n^{\text{atoms}} \frac{\partial E_n}{\partial r_{i\alpha}} \ , \tag{4.56}$$

where $f_{i\alpha}$ is the α:th component of the force and the summation runs over atoms within the predefined cutoff radius [88].

One of the valuable aspects of the gaussian approximation potentials is that, since it is possible to calculate the error estimates for the predictions, the accuracy of the model can be tuned to have errors within some tolerance [94]. If certain atomic configurations are underrepresented in the data set, more input data can be added.

The gaussian approximation potentials provide a good compromise between the accuracy of DFT and the efficiency of MD: when used in MD simulations the computations can be atleast 2 orders of magnitude faster than DFT calculations yet the accuracy can be very close [16, 94]. When comparing to other MD potentials, such as EAM and Tersoff-type potentials, GAPs are typically 2-3 orders of magnitude slower.

5. Methods

5.1 Training data

The training data set was made by constructing the simulation boxes with the ASE package [95] in python and computing the energies with DFT. The DFT calculations were conducted using the VASP software [68] with the PBE GGA exchange-correlation functional [96]. For W, Mo and Ta the number of valence electrons used in computations were 14, 14 and 11 respectively and the core electrons were treated with Projector-Augmented Wave (PAW) method [69]. The cutoff energy for plane-waves was 500 eV and the first Brillouin zone was integrated using a Monkhorst-Pack grid [97] with constant maximum spacing of 0.15 Å^{-1}. The rest of the VASP INCAR parameters used in DFT calculations are listed in table 5.1 below.

The systems for the training database were chosen so that the atomic environ-

INCAR Tag	Value
ENCUT	500.0
KSPACING	0.15
SIGMA	0.10
EDIFF	1.00e-06
GGA	PE
PREC	Accurate
ISMEAR	1
KPAR	2
NELM	100
NELMIN	4
NCORE	20
LASPH	.TRUE.
LWAVE	.FALSE.

Table 5.1: INCAR options used in DFT calculations of the training database.

ments would contain a lot of variety but still being realistic and relevant for the possible simulations to be made with the potential. The training dataset included also pure systems, constructed by Byggmästar et al. [17, 89], containing only one element for all used elements W, Mo and Ta. The single atom systems include many different atomic configurations such as distorted crystal structures with different cell volumes, vacancies, self-interstitials and surfaces. To capture the interaction at shorter interatomic spacings, short-range structures are also included, which is a BCC configuration with a randomly added atoms between the lattice sites. The details of these systems can be found in [17] and [89].

Multi-atom systems consisted of simulation boxes with all three elements (Mo, Ta, W) in different concentrations ranging from 10/10/80 at. % to equi-atomic concentrations. Also the atomic compositions are permuted so that each atom type has similar concentrations and the ordered systems are done with 3 different lattice constants. Lattice constants used for distorted BCC and single vacancy alloy systems are 3.0, 3.2 and 3.4 Å and for short-range configurations 3.15, 3.225 and 3.3 Å. The disordered liquid systems were done by running MD simulations with preliminary GAPs made using distorted BCC structures as training data and were prepared with different densities. The liquid surface structures with 3 elements include also BCC (100) surfaces as they were made by fixing two layers of atoms in place from the other edge of the surface slab when the MD simulations were run. Also, because it is important for the repulsive part of the potential (4.55) to be smoothly connected to the GAP part, dimer structures with all possible atom pairs (6) and with multiple distances are included in the training database. The dimers have interatomic distances ranging from short distances (1.2 Å) to interatomic distances close to equilibrium distances.

Since almost all of the atoms in multi-component systems have different environments, especially in the disordered phases, not as many systems were included. Also the sparsification algorithm takes care that the chosen representative data points differ from each other so that including excessive amounts of single atom systems should not have much effect on the final training dataset, since the number of sparse points used is much less than the amount of different atomic environments. In the multi-atom configurations most of the environments are in disordered liquid phase, since these structures contain a lot of variety in the environments. The number of simulation boxes for training database are given in the table 5.2.

5.2 Details of the potentials

The GAP-software [16] contains multiple possible descriptors and covariance functions and the ones used in this work are the two-body descriptor with squared exponential

	Single element		Mo-Ta-W alloy	
Configuration type	N_{system}	N_{atoms}	N_{system}	N_{atoms}
Isolated atom	3	1	-	-
Dimer	46	2	45	2
Distorted lattices:				
BCC	7581	1-2	84	54
BCC (high temp)	120	54	-	-
FCC	300	1	-	-
HCP	300	2	-	-
A15	300	8	-	-
C15	300	6	-	-
dia	300	2	-	-
SC	300	1	-	-
Surfaces:				
BCC (100)	135	12	-	-
BCC (110)	135	12	-	-
BCC (111)	125	12	-	-
BCC (112)	135	12	-	-
Liquid surfaces	72	128, 144	61	128
γ	534	12	-	-
Vacancies:				
single vacancy	630	53	30	53
di-vacancy	30	118	-	-
tri-vacancy	43	117	-	-
Self-interstitials (SIA):				
single-SIA	96	121	-	-
di-SIA	43	122, 252	-	-
Other structures:				
Short-range	266	53-55	20	53
Liquids	135	128	61	128

Table 5.2: Systems used as training database for GAPs. N_{system} is the total number of systems for each configuration and N_{atoms} is the number of atoms in each system. Single atom type systems are approximately equally distributed between each atom type (Mo, Ta and W). Multi-atom type systems are distributed between different compositions with atomic concetrations ranging from 10/10/80 at.% to equi-atomic concentrations.

covariance function (4.45) and the SOAP descriptor in (4.49) with the dot-product kernel (4.52). The effect of including also three-body descriptor to a single atom type potential for tungsten was investigated in [17] and was shown to give only a minor increase in accuracy and is therefore not included in the potentials made in this work. Multiple potentials were trained using different number of sparse points to evaluate the effect of number of training data points to accuracy and efficiency of the potential. This could be helpful for future reference when deciding the amount of sparse points used in training as well as the number of environments needed in the training database.

Many of the fitting parameters were tested by Byggmästar et al. in [17] and were obtained directly from their results, which is reasonable due to the similarity of the atom types that are simulated. The two-body GAP parts were trained consistently with 20 sparse points (i.e. interatomic distances) from the training database, which consisted of more than 10^5 and 10^6 descriptors for symmetric and asymmetric dimer pairs respectively. For the SOAP descriptor 7 different values were used: 250, 500, 1000, 2000, 3000, 4000 and 5000 sparse points for each atom type, when the total number of SOAP descriptors (i.e. number of atoms) found in the training data was 159268 for all three elements. The total number of descriptors found by the GAP software in the training database is listed in table 5.3.

	Descriptors	Partial derivatives
Two-body:		
Mo-Mo	1287478	9531276
Ta-Ta	1217278	8892228
W-W	1249740	9237144
Mo-Ta	112708	676248
Mo-W	125540	753240
Ta-W	124520	747120
SOAP:		
Mo	53469	5313957
Ta	53198	4992078
W	52601	5181441

Table 5.3: Total number of descriptors and their partial derivatives included in the training database for both two-body and SOAP descriptors. The atoms listed for SOAP are the central atoms of the descriptors.

The cutoff distance for both descriptor types was set to 5 Å with cutoff transition distance of 1Å, and were both also obtained from [17] by testing various values. Training parameters for SOAP in (4.49) are for $n_{\max}$ and $l_{\max}$, which give the cutoff values for

maximum n and l for the spherical harmonics in the expansion, and the chosen value for both was 8 as in [17]. The ζ parameter in (4.48) was chosen to be 4. The assumed errors σ_ν in the training data, which act also as regularization parameters, were likewise adopted from Byggmästar et al. and are listed with rest of the GAP parameters in table 5.4 for both descriptor types. The parameter δ is a scaling parameter as in (4.52) and is also added for two-body descriptor. The sparse method is the sparsification algorithm used for each descriptor type and were chosen as CUR decomposition [93] and uniform methods for SOAP and two-body descriptors respectively. The σ_{atom} parameter gives the width or the standard deviation for the gaussians projected onto atomic positions in SOAP-descriptor, σ_{jitter} is a small parameter added to the sparse covariance matrix to make the computations numerically stable [88].

	General		
σ_{jitter}	10^{-8}		
σ_ν:	Energy (meV/atom)	Force (eV/Å)	Stress (eV)
Default	0.001	0.04	0.04
Liquid	0.01	0.4	-
Liquid surface	0.01	0.2	-
Dimer	0.01	0.4	-
γ-surface	0.002	0.08	-
Short range	0.01	0.4	-
	Two-body	SOAP	
n_{sparse}	20	250-5000	
r_{cut}	5.0 Å	5.0 Å	
Δ_{cut}	1.0 Å	1.0 Å	
δ	10.0 eV	2.0 eV	
Covariance	ard_se	dot_prod.	
Sparse method	uniform	CUR	
σ_{atom}	-	0.5 Å	
l_{max}	-	8	
n_{max}	-	8	
ζ	-	4	

Table 5.4: Training parameters for the GAP software used in the developed potentials. σ_{jitter}: a small value used in regularisation, σ_ν: regularisation parameters, n_{sparse}: number of sparse points, r_{cut}: cutoff distance, Δ_{cut}: cutoff transition width, δ: scale parameter, Covariance: covariance functions used for descriptors (ard_se is squared exponential and dot_product is the SOAP dot-product kernel), Sparse method: sparsification algorithm, σ_{atom}: standard deviation of Gaussians projected onto atoms in SOAP, l_{max} & n_{max}: parameters for the expansion in 4.49, ζ: SOAP kernel parameter (4.48).

The repulsive part of the potential in (4.55) was chosen to be a ZBL-type [75] screened coulomb potential as in (4.11) with a separately fitted screening function for all atom type pairs. The data for the fitted screening functions were calculated using DFT DMol for all electrons in [98]. The repulsive pair potential is of the form

$$V_{\text{pair}}(r) = V_{\text{ZBL}}(r) f_{\text{cut}}(r) \ , \tag{5.1}$$

with the cutoff function

$$f_{\text{cut}}(r) = \begin{cases} 1 & , \ r \leq r_1 \\ 1 - \chi^3(6\chi^2 - 15\chi + 10) & , \ r_1 < r < r_2 \\ 0 & , \ r \geq r_2 \ , \end{cases} \tag{5.2}$$

where $\chi = (r - r_1)/(r_2 - r_1)$, $r_1 = 1.0$ Å and $r_2 = 2.2$ Å similarly to [17].

5.3 Running simulations

The GAPs were trained using the QUIP software package [99] in a computing cluster. The disordered systems in the training database as well as test MD simulations were done using the LAMMPS software [100, 101]. LAMMPS was compiled with QUIP and the GAP package was added to QUIP library. When training the GAP, the training database was contained in a single input file with another input file containing the data for the repulsive pair potential. Some unseen atomic environments for GAP were contained in a separate input file as a test database and errors were calculated for both training and test data separately for each potential.

After training, the GAP software provides output files for each type of descriptor, which in this work consists of 6 types of 2-body and three SOAP descriptors: one two-body for each atom type pair and one SOAP for each atom type. GAP also provides a separate output file containing the pair potential data and the coefficients in 4.55. When running MD simulations with LAMMPS using GAPs the potential files are then given as input files via the QUIP package.

6. Results

Several potentials were developed for Mo-Ta-W concentrated alloy systems in order to study the accuracy dependence on the number of sparse points. The accuracy of the potentials was tested on both the training set and on a separate testing data set, from which no data were included in the training set. The test set consists of 1284 systems some containing only single atom type but most contain two or three atom types. The

	Single element		Alloy (Mo,Ta,W)	
Configuration type	N_{system}	N_{atoms}	N_{system}	N_{atoms}
Distorted lattices:				
BCC 1	-	-	36	54
BCC 2	-	-	36	54
Stress	2	54	189	53-54
Phonon (BCC high temp)	22	54	187	54
Surfaces:				
BCC (100)	-	-	90	54
BCC (110)	-	-	90	108
BCC (111)	-	-	90	153
Liquid surfaces	-	-	38	128
Vacancies:				
Single vacancy	-	-	190	53
Self-interstitials (SIA):				
Single-SIA	-	-	90	121
Other structures:				
Short-range	-	-	16	55
Liquids	20	54	188	54

Table 6.1: Test system database configuration types.

multi-atom type systems have configuration types ranging from distorted BCC, ordered and liquid surface, self-interstitial, vacancy, liquid and short-range structures. Most of

the multi-atom configurations in the test set consist only of two atom types (Mo and W) and the only configuration types containing three atom type systems are distorted BCC lattices (BCC1 and BCC 2), liquid surfaces and short range systems. Many of the two atom type systems contain only a small fraction of the other atom type and are therefore close to single atom type systems with respect to atomic environments. The lattices in BCC 2 are more distorted than in BCC 1 and the stress configuration type consists of deformed BCC lattice structures. The number of each test environment is given in the table 6.1.

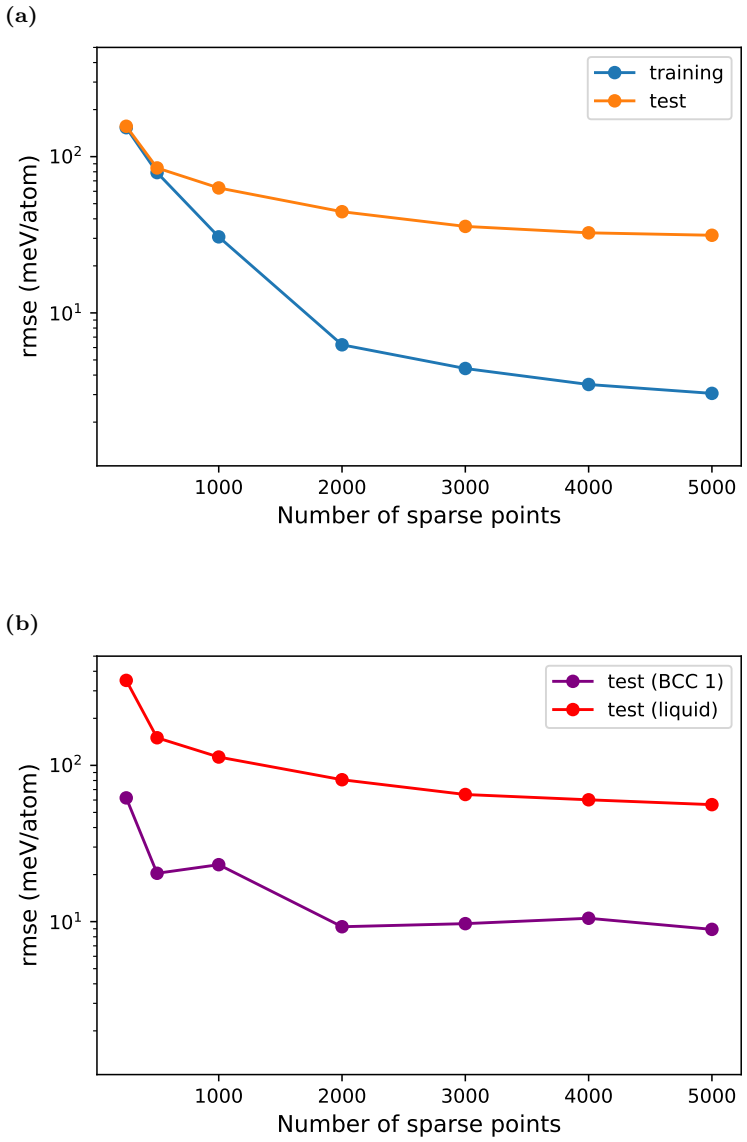

Figure 6.1: (a): Root mean square errors of potential energies with respect to DFT calculated with different GAPs. (b): Test set RMSE of potential energies with respect to DFT calculated for only certain configuration types (BCC 1 and liquid).

Both the test and training errors of energy can be seen to converge with increasing number of sparse points from figure 6.1a. The root mean square errors of training data for almost all configuration types range from < 1 meV/atoms to few meV/atom for GAPs trained with >2000 sparse points, which is consistent with the given parameters in 5.2. Only dimer systems had training errors in the range of 20-30 meV/atom. Also, even though a large number of sparse points was used in training some of the potentials, no overtraining is seen as the test error decreases with increasing number of sparse points. The total RMSE for the test data set converges close to 30 meV/atom with large n_{sparse}.

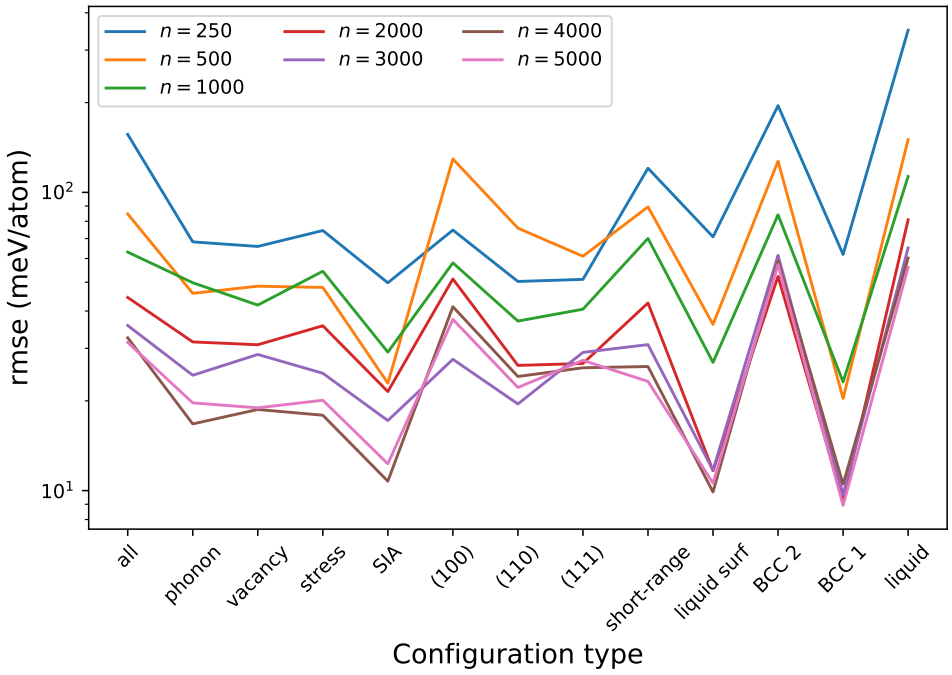

Figure 6.2: RMS errors vs different configuration types for the test database. n is the number of sparse training points.

The magnitude of the errors depends also on the type of the atomic configuration as can be seen from figure 6.2. Since the training database consisted of a lot of disordered structures and systems with short interatomic distances, the smallest test errors were obtained for SIA, liquid surface and BCC 1 structures, when the GAP used >2000 sparse points.

6.1 Dimer energy

Since the repulsion at extremely short interatomic distances is taken care of by the fitted ZBL-type pair potential, the training data should make a significant contribution only at interatomic distances closer to equilibrium distances. Therefore ideally, the GAPs

should predict energies relatively close to zero in comparison to the repulsive part at short distances, when no distinct pair potential is used in training.

As with other tests, the dimer potential energies predicted by GAP were decent when the GAP was trained with at least 3000 sparse points. Then all of the dimer potential energies show a smooth transition from further distances to the highly repulsive shorter interatomic distances. Also the energies calculated with a GAP trained without pair potential predicts energies that are insignificant compared to the ZBL-type potential at extremely short distances. The potential energies for all dimer pairs are shown in figure 6.3.

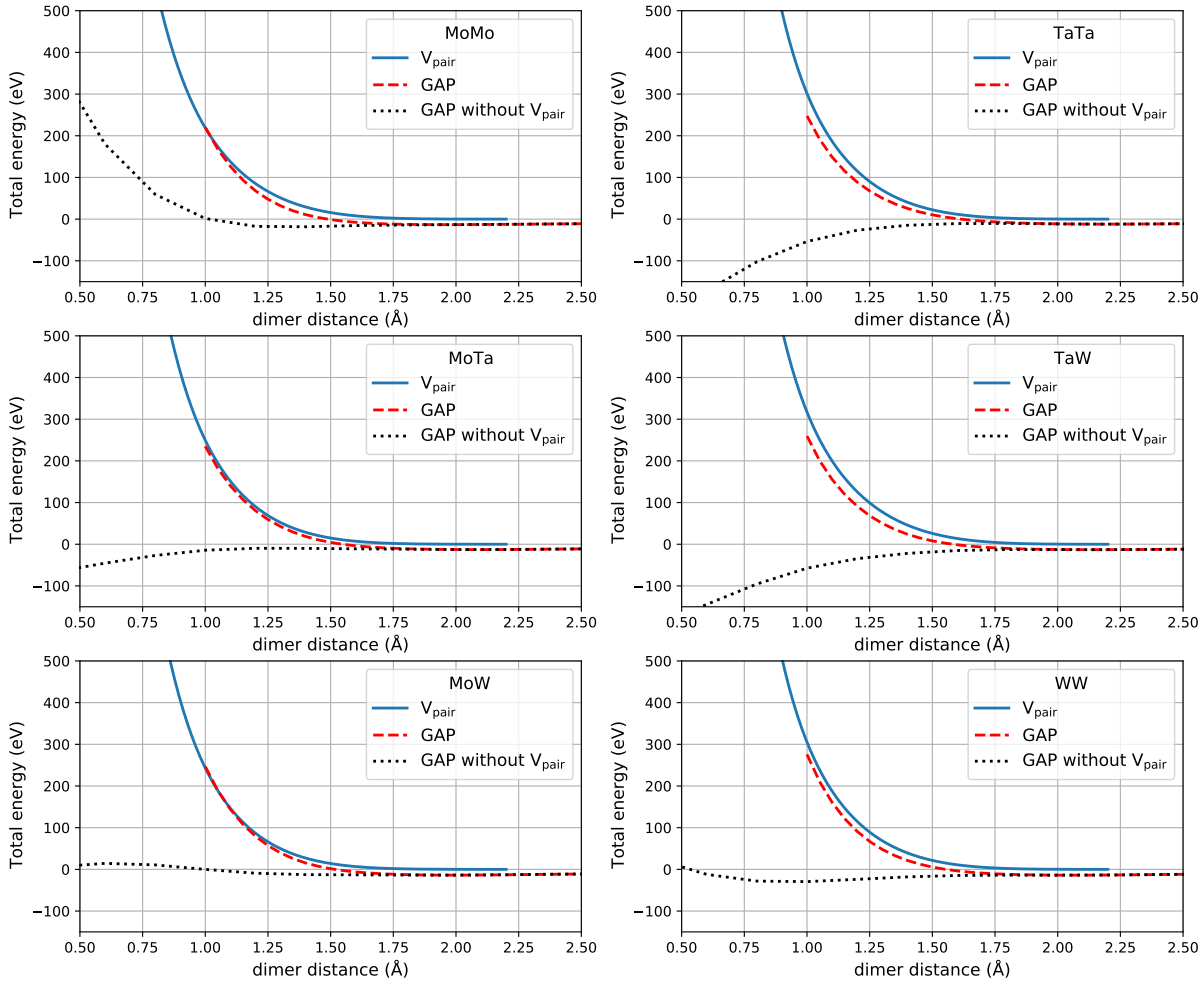

Figure 6.3: Dimer energies calculated with GAP trained with 3000 sparse points. V_{pair} is the repulsive ZBL-type pair potential, the red line is the potential energy predicted by GAP and the dashed black line is the GAP prediction without the repulsive pair potential.

When comparing the dimer potential energy at a range between 1.5 Å and the equilibrium distances, it can be seen from figure 6.4, that the GAP with less sparse training points shows significant discrepancy in the Mo-Ta dimer energy. Other dimer pairs did not show similar behaviour with a potential trained over less sparse data points.

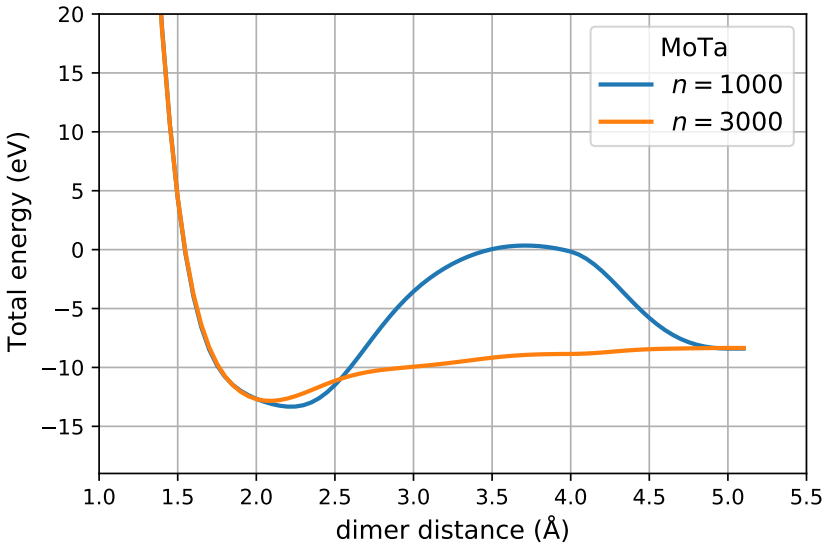

Figure 6.4: Dimer potential energy for Mo-Ta system calculated with different GAPs.

6.2 Bulk properties

The potentials were validated also by calculating energy-volume curves for different compositions of Mo-Ta-W alloys as well as pure Mo, Ta and W systems. Details of the atomic concentrations of the systems are given in table 6.2 an atoms in the systems were randomly ordered. Even with a moderate number of sparse data points, the GAP potentials predict values really close to the values obtained from DFT. The curves for different generated potentials are shown in figure 6.5.

System	Mo %	Ta %	W %
Vol_0	20.4	20.4	59.3
Vol_1	20.4	40.7	38.9
Vol_2	20.4	61.1	18.5
Vol_3	40.7	20.4	38.9
Vol_4	40.7	40.7	18.5
Vol_5	61.1	20.4	18.5

Table 6.2: Multi-atom type systems used in Energy-Volume curve calculations. Values given in the table are atomic percentages for each element.

The minima of the energy-volume curves are reproduced with high success by GAPs with $n_{\text{sparse}} \geq 1000$, but some differing is seen further away from the minima. The potential trained with only 250 sparse points shows noticable differences in energy-volume curves and the volume minima with respect to the DFT calculations. Deviation from the DFT values far from the minima is to be expected for all developed potentials, since the

training data consists mostly of systems with lattice constants close to the minima. Also the energy-volume plots show that the mixtures of the three elements (Mo,Ta,W) have both their energy and volume minima close to average of the corresponding values for the pure constituent elements.

Some test simulations were also done using one of the generated GAPs and to produce as accurate results as possible without extensively losing efficiency, GAP with

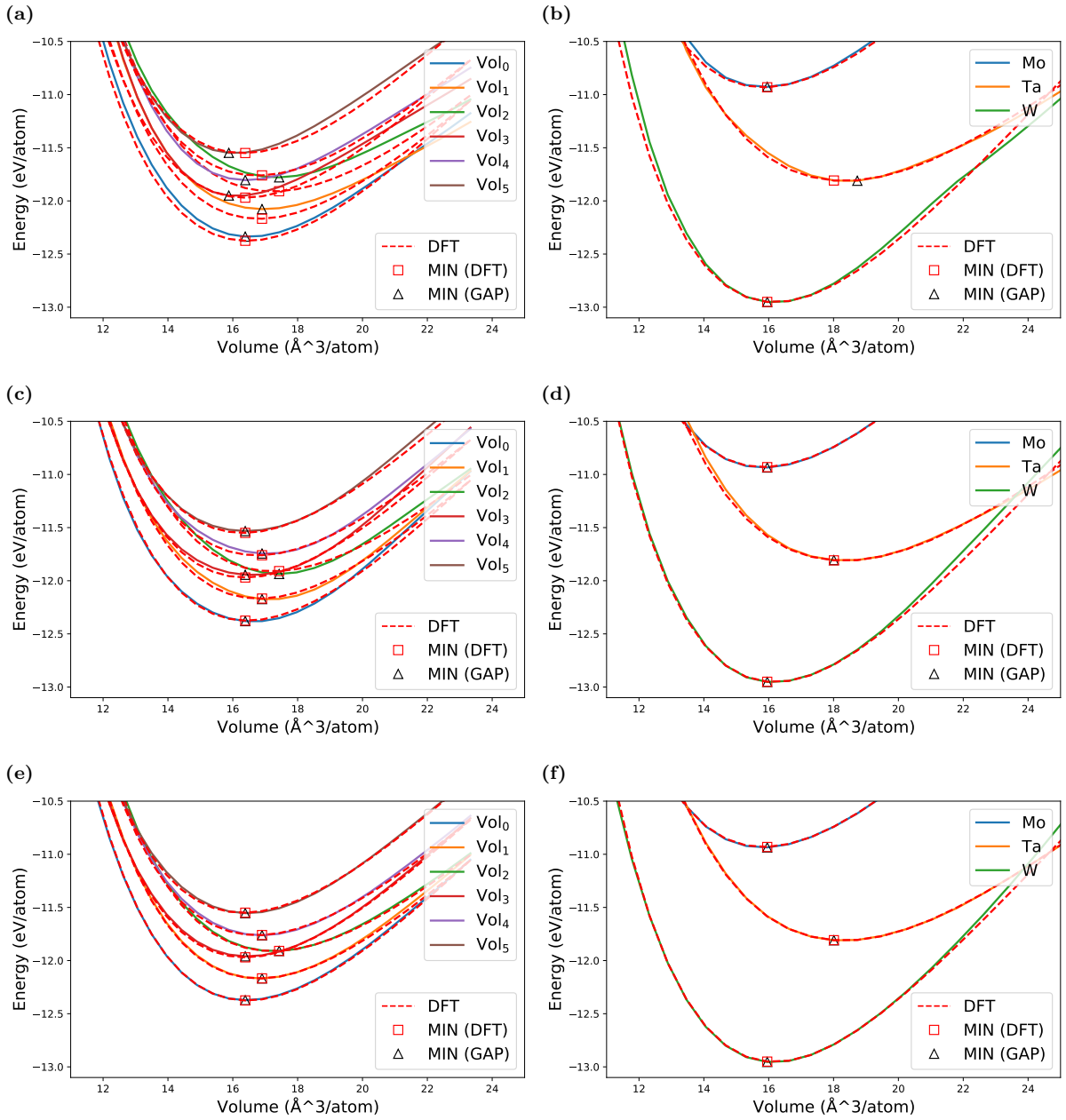

Figure 6.5: Energy-Volume curves for Mo-Ta-W alloy systems with different compositions and pure single atom systems calculated with different GAPs and DFT. In figures (a), (c) and (e) are E-V curves for multi-atom systems calculated with GAPs having 250, 1000 and 3000 sparse training points respectively. Figures (b), (d) and (f) are the corresponding curves for single-atom systems

$n_{\text{sparse}} = 4000$ was chosen. Bulk simulations were done with 4 different compositions each containing 250 atoms in a BCC lattice with lattice constant 3.2 Å and were run for $\sim$ 500000 timesteps with a 0.003 ps timestep (total time 1.5 ns). The test MD simulation systems contain one with equi-atomic concentrations and three systems with concentrations of 60/20/20 at.% with different compositions. Periodic boundary conditions were applied in all three dimensions. The systems were first heated within 35000 timesteps from nearly 0 K to 5000 K to see how they would behave while changing from solid to liquid phase. Then the simulation boxes were immediately cooled again to very low temperature within 500 000 timesteps. All of the systems liquified and solidified back to BCC lattice with some defects and volumes per atom between 16.7-17.5 Å^3. The total potential energies of the simulation systems were either slightly higher (less than 50 eV) or almost exactly equal to the starting potential energy. The potential energy curve for the heating and cooling parts of the simulation system with 60 at.% Ta is shown in figure 6.6. The figure shows phase transitions at around 4000 K (melting) and 2000 K (recrystallization). Due to the extremely fast cooling, some defects are very likely to remain in the lattice which may cause the system being at slightly higher potential energy in the cooling phase.

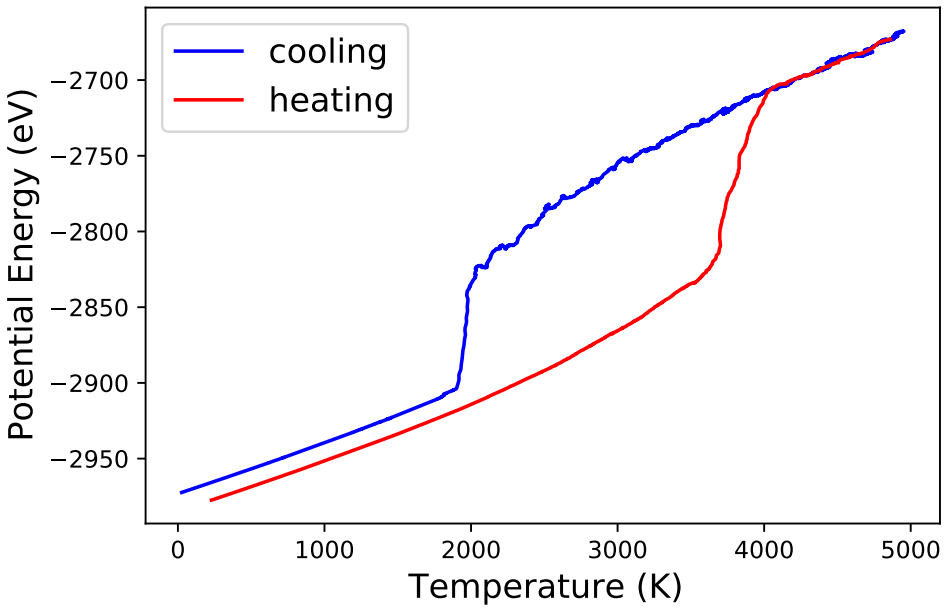

Figure 6.6: Running average of the total potential energy vs temperature. Red is the heating part starting from near 0 K and ending close to 5000 K and blue is the cooling part of the simulation.

6.3 Surface properties

The generated GAPs performance over surface simulations was tested by calculating surface energies of (100), (110) and (111) surfaces with DFT for systems with different atomic

compositions. The surface energy can be defined as

$$\gamma = \frac{E_{\text{surface}} - E_{\text{bulk}}}{2A} = \frac{E_{\text{surface}} - E_{\text{ref}} N_{\text{atom}}}{2A} \ , \tag{6.1}$$

where E_{surface} and E_{bulk} are energies for the surface and the bulk structures respectively and A is the surface area. E_{ref} is then the reference energy per atom in a minimized bulk system and N_{atom} is the number of atoms in the surface system. To obtain the lattice parameters for systems with different concentrations and the reference energies, the DFT calculations were first done by relaxing a bulk simulation box for each composition and surface direction. Then a vacuum of 30.0 Å was added to the surface direction and the atom positions were minimized. The parameters for VASP DFT calculations were otherwise the same as for making the training database except the added parameters: EDIFFG $= -0.01$, IBRION $= 2$, ISIF $= 3$, NSW $= 50$ for bulk relaxation. For the surface structure minimization only ISIF was changed to 2. EDIFFG parameter gives the break condition for the relaxation loop, so that when all forces are smaller than (the negative) of the given value, the relaxation is finished. The ISIF parameter defines the degrees-of-freedom for the system (with respect to atom positions, cell shape and cell volume) and whether both forces and stress tensor are calculated. The IBRION parameter defines the computational method for the relaxation/simulation and NSW is the maximum number of iterations for the simulation.

The surface energies were computed similarly using the developed GAPs and the results are compared in figure 6.7. The figure shows both the surface energies calculated with GAPs with different number of sparse points and the absolute values of the residuals for 4 simulations systems with different atomic compositions. The systems for surface energy calculations had one equi-atomic concentrated system and three approximately 60/20/20 at.% systems with different compositions similarly to the bulk test simulation systems.

It can be seen from the results that the number of sparse points has a significant effect on the performance of the potential in terms of surface properties. With only 1000 sparse points for each atom type, the potential not only had greater error in the surface energy but was also unable to reproduce the order of the surfaces with respect to energy when compared to DFT. This is a major drawback for the potential and would possibly lead to unphysical results when used for systems containing surfaces. Potentials with larger n_{sparse} were able to predict the same surface as minimum as DFT calculations yet still had largest residuals of 25 meV/Å($n_{\text{sparse}} = 4000$) and 20 meV/Å($n_{\text{sparse}} = 5000$). The differences in the performances of the potentials are quite small, which shows that using too many sparse training points may only cause the potential to be inefficient and not necessarily more accurate as most likely would be the case if even larger n_{sparse} was used. The DFT calculated surface energies for different compositions are highest for the

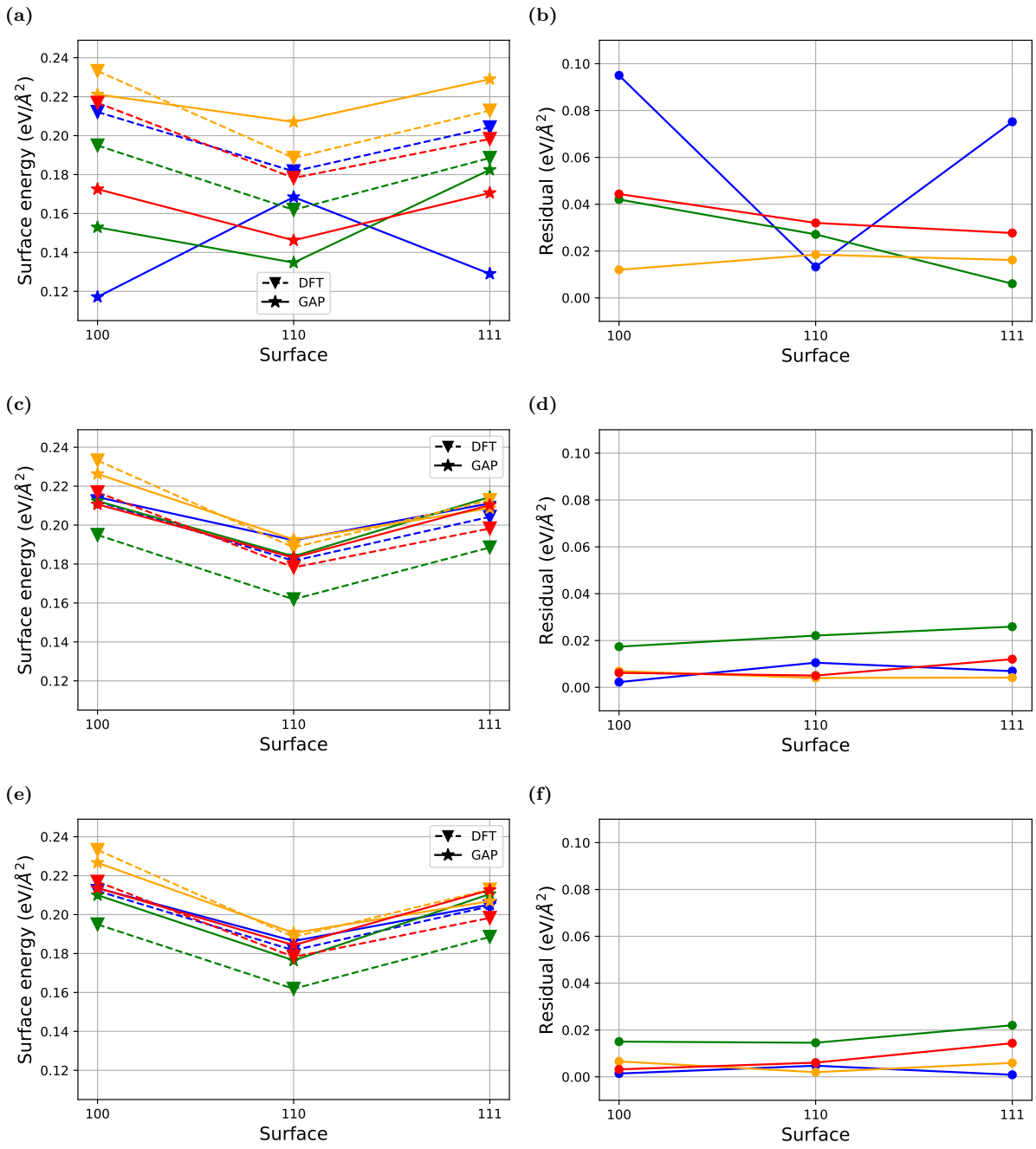

Figure 6.7: Figures (a), (c), (e): Surface energies of different Mo-Ta-W compositions calculated with DFT and the developed GAPs with different n_{sparse}: (a) 1000, (c) 4000, (e) 5000. (b), (d), (f) corresponding residuals of surface energies. Green: 60/20/20 at.% Ta/Mo/W, Yellow: 60/20/20 at.% W/Mo/Ta, Red: 60/20/20 at.% Mo/Ta/W, Blue: equi-atomic concetrations.

system with mostly W atoms and lowest for the system with mostly Ta atoms, as expected when comparing to single atom systems in [89].

The properties of the GAPs were also tested by running test MD simulations for surface structures. Simulations were performed for 4 systems with different compositions using the potential trained with 4000 sparse points for each atom type. All systems had

360 atoms and atomic concentrations similar to the systems in surface energy calculations. All structures started as perfect BCC lattices with two (100) surfaces. As in the bulk test MD simulations, the surface boxes were first heated from nearly 0 K to 5000 K within 35000 steps with a timestep of 0.003 ps and then cooled with >500 000 steps. Periodic boundary conditions were applied on the x and y -axes. Due to technical issues the MD simulation runs had to be restarted multiple times and the number of steps in the cooling part was changed simultaneously for some systems, since the test runs were only meant to show how the systems behave under the simulations and the exact numbers are not meaningful.

Three of the surface systems cooled to disordered local minimum energy states, that were higher in energy than the original lattice structures and the formations resemble the so called metallic glass states. One of the systems was run after the stabilization at 1700 K for approximately 450 000 steps to see whether it would undergo a phase transition, but the system remained at a similar conformation with almost static total potential energy. One of the test surface systems however, cooled to a slightly lower energy state with BCC lattice structure and a lattice direction of (111) at surfaces, even though both surfaces of the slab showed some roughness. This is reasonable since the (111) has a lower surface energy than (100) although the (110) surface has even lower surface energy as can be seen from figure 6.7. The potential energy vs temperature curve and the final frame of the system are shown in figure 6.8a and 6.8b. The white atoms in the simulation box image are the atoms at the surface layer and the blue atoms are recognized as atoms in BCC lattice conformation by common neighbour analysis. The image was rendered using Ovito-software. The potential energy vs temperature curve show phase transitions at approximately 3000 K (heating) and 2000 K (cooling).

The results obtained for validating the developed potentials are physically reasonable. The test simulations were conducted with an extremely rapid decrease in temperature, which can result in the formation of metallic glass also in real systems. Also the recrystallization to a lower-energy surface is physically reasonable. The trained GAPs produce sensible results when enough sparse data points were used in training.

(a)

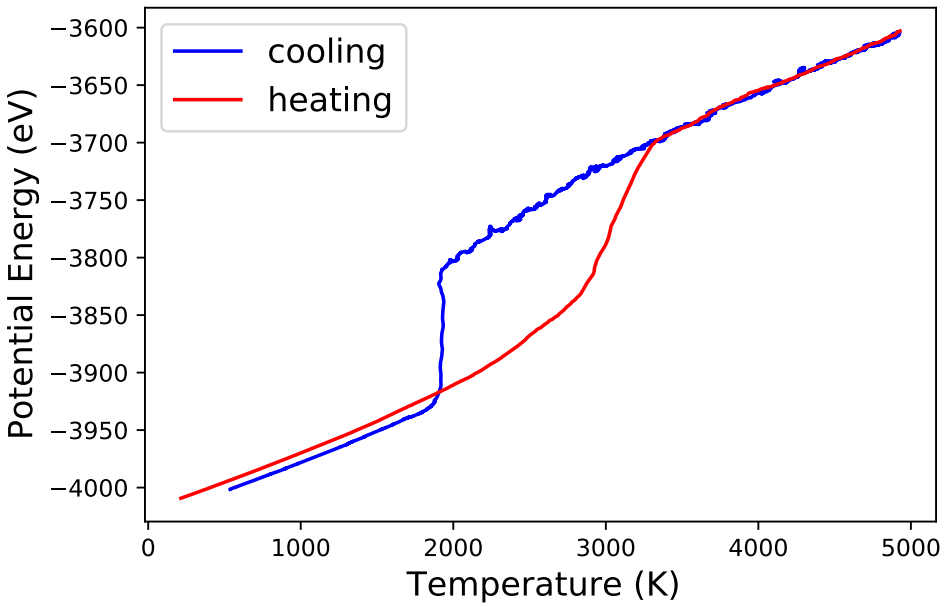

(b)

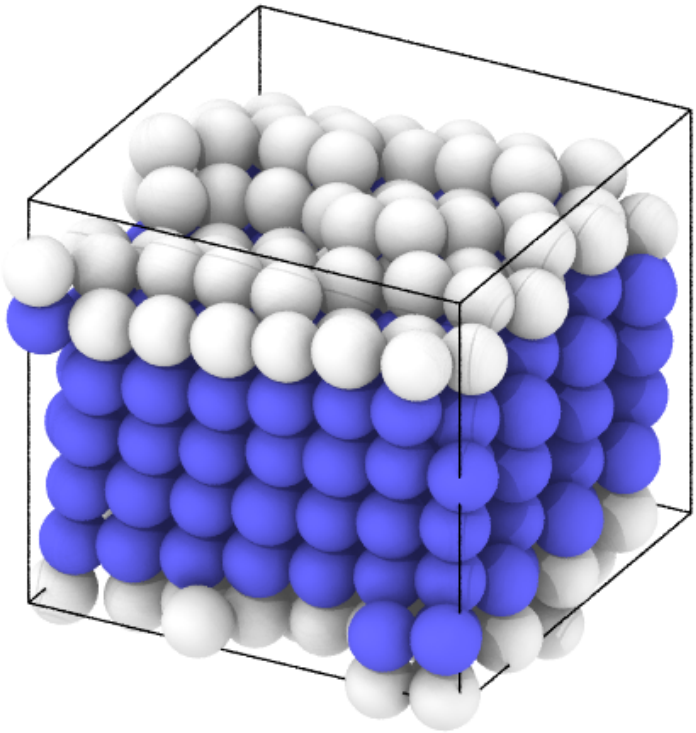

Figure 6.8: (a): Running average of total potential energy vs temperature of the simulation system. Red is a quick heating part and blue is a slower cooling part of the simulation. (b): Final frame of one of the surface simulation boxes. The simulation system ended in a BCC lattice configuration with rough surfaces with normals in (111) lattice direction. The starting point was a perfect BCC lattice with (100) surfaces.

7. Summary

Finding new efficient and sustainable methods to produce electricity has become one of the major problems for the world's energy engineers to solve due to the increasing energy consumption. Nuclear fusion reactors have been under examination as a competent alternative for energy production compared to fossile fuels and other major sources. Over the last few decades the research and development for fusion power plants has taken major leaps forward with large global projects such as JET and ITER. Fuel for nuclear fusion power plants is extensively available, yet the large challenges regarding the materials of the plasma-facing components need to be sorted out in order for the energy released from fusion reactions to be harnessed for electricity. Tungsten (W) has been the principal material so far, yet the properties are still far from optimal. High-entropy alloys (HEA) have shown promising characteristics for such applications and have been under investigation for the past decade.

In this work, interatomic potentials for Mo-Ta-W concentrated alloys for molecular dynamics simulations were developed using the GAP framework (Gaussian approximation potentials). The GAPs were trained using a large training database consisting of pure single atom systems and multi-atom type systems (Mo, Ta, W) with energies calculated with DFT (VASP-software). The training database contains multiple configuration types and a lot of systems with varying interatomic distances for the potentials to have possible use in high-energy and radiation simulations.

The accuracy of the developed potentials was tested on a separate testing database. All GAPs used same descriptors and parameters except for the number of sparse training data points. The number of sparse points used range from 250 to 5000 for each atom type and the accuracy over both the training set and test set converged with respect to n_{sparse}. The results show that using larger number of sparse points does not necessarily increase the accuracy, yet may cause the potential to become needlessly inefficient.

The performance of the potentials was also tested for bulk materials and surface structures. The developed GAPs were able to produce the energy-volume curves accurately for different Mo-Ta-W concentrated alloy compositions as well as pure single element systems, when the number of sparse training points was ≥ 1000. Some test simulations were also conducted to see whether some unphysical phenomena would occur and

the results obtained show reasonable behaviour. Surface energy calculations using GAPs showed that the performance can be quite poor when not enough data is given while training the potentials, but the overall results show promising possibilities.

The developed GAPs seem to perform generally well although more validation might be needed before the potentials are used for heavy duty computations. Also, if the focus would be to create potentials for three element Mo-Ta-W alloys only, the training database should consist of a lot greater proportion of multi-component systems.

References

[1] IEA. World energy outlook 2020. https://www.iea.org/reports/world-energy-outlook-2020, 2020.

[2] Chuanjun Huang and Laifeng Li. Magnetic confinement fusion: a brief review. *Frontiers in Energy*, 12(2):305–313, June 2018. PT: J; NR: 37; TC: 0; J9: FRONT ENERGY; SI: SI; PG: 9; GA: GJ5LM; UT: WOS:000435422700010.

[3] Jochen Linke, Juan Du, Thorsten Loewenhoff, Gerald Pintsuk, Benjamin Spilker, Isabel Steudel, and Marius Wirtz. Challenges for plasma-facing components in nuclear fusion. *Matter and radiation at extremes*, 4(5):056201–18, Sep. 2019.

[4] J. Knaster, A. Moeslang, and T. Muroga. Materials research for fusion. *Nature physics*, 12(5):424–434, May 3, 2016.

[5] Tielong Shen, Yong Dai, and Yongjoong Lee. Microstructure and tensile properties of tungsten at elevated temperatures. *Journal of nuclear materials*, 468:348–354, Jan. 2016.

[6] Steffen Antusch, Jens Reiser, Jan Hoffmann, and Alexandru Onea. Refractory materials for energy applications. *Energy technology (Weinheim, Germany)*, 5(7):1064–1070, July 2017.

[7] S. Nagata, B. Tsuchiya, T. Sugawara, N. Ohtsu, and T. Shikama. Helium and hydrogen trapping in w and mo single-crystals irradiated by he ions. *Journal of nuclear materials*, 307:1513–1516, 2002.

[8] W. M. Shu, G. N. Luo, and T. Yamanishi. Mechanisms of retention and blistering in near-surface region of tungsten exposed to high flux deuterium plasmas of tens of eV. *Journal of nuclear materials*, 367:1463–1467, 2007.

[9] Stéphane Gorsse, Jean-Philippe Couzinié, and Daniel B. Miracle. From high-entropy alloys to complex concentrated alloys. *Comptes rendus. Physique*, 19(8):721–736, Dec. 2018.

[10] F. Granberg, K. Nordlund, Mohammad W. Ullah, K. Jin, C. Lu, H. Bei, L. M. Wang, F. Djurabekova, W. J. Weber, and Y. Zhang. Mechanism of radiation damage reduction in equiatomic multicomponent single phase alloys. *Physical review letters*, 116(13):135504, Apr. 2016.

[11] Takeshi Nagase, Philip D. Rack, Joo Hyon Noh, and Takeshi Egami. In-situ TEM observation of structural changes in nano-crystalline CoCrCuFeNi multicomponent high-entropy alloy (HEA) under fast electron irradiation by high voltage electron microscopy (HVEM). *Intermetallics*, 59(C):32–42, Apr. 2015.

[12] O. El-Atwani, N. Li, M. Li, A. Devaraj, J. K. S. Baldwin, M. M. Schneider, D. Sobieraj, J. S. Wróbel, D. Nguyen-Manh, S. A. Maloy, and E. Martinez. Outstanding radiation resistance of tungsten-based high-entropy alloys. *Science advances*, 5(3):eaav2002, Mar. 2019.

[13] Stanley Chang, Ko-Kai Tseng, Tzu-Yi Yang, Der-Sheng Chao, Jien-Wei Yeh, and Jenq-Horng Liang. Irradiation-induced swelling and hardening in HfNbTaTiZr refractory high-entropy alloy. *Materials letters*, 272:127832, Aug. 2020.

[14] D. C. Rapaport. *The Art of Molecular Dynamics Simulation*, volume 2nd ed. Cambridge University Press, Cambridge, UK, 2004. ID: Accession Number: 304477.

[15] Chandler A. Becker, Francesca Tavazza, Zachary T. Trautt, and Robert A. Buarque de Macedo. Considerations for choosing and using force fields and interatomic potentials in materials science and engineering. *Current Opinion in Solid State and Materials Science*, 17(6):277–283, 2013. ID: 272101.

[16] Albert P. Bartók, Mike C. Payne, Risi Kondor, and Gábor Csányi. Gaussian approximation potentials: The accuracy of quantum mechanics, without the electrons. *Physical review letters*, 104(13):136403, Apr. 2010.

[17] J. Byggmästar, A. Hamedani, K. Nordlund, and F. Djurabekova. Machine-learning interatomic potential for radiation damage and defects in tungsten. *Physical Review B*, 100(14), Oct. 2019.

[18] Friedrich Wagner. Fusion energy. *Mrs Energy & Sustainability*, 5:e8, June 2018. PT: J; NR: 21; TC: 0; J9: MRS ENERGY SUSTAIN; PG: 16; GA: GL2LA; UT: WOS:000436951200001.

[19] EUROfusion. JET history. https://www.euro-fusion.org/devices/jet/jet-history, 2020.

[20] D. J. Campbell. The first fusion reactor: ITER. *Europhysics news*, 47(5-6):28–31, Sep. 2016.

[21] ITER Organization. The ITER story. https://www.iter.org/proj/iterhistory, 2020.

[22] A. J. H. Donné. The european roadmap towards fusion electricity. *Philosophical transactions of the Royal Society of London. Series A: Mathematical, physical, and engineering sciences*, 377(2141):20170432, Mar. 2019.

[23] G. Federici. Plasma wall interactions in iter. *Physica scripta*, 2006:1–8, May 2006.

[24] Kun Wang, R. P. Doerner, M. J. Baldwin, F. W. Meyer, M. E. Bannister, Amith Darbal, Robert Stroud, and Chad M. Parish. Morphologies of tungsten nanotendrils grown under helium exposure. *Scientific reports*, 7(1):42315, Feb. 2017.

[25] Mario Merola, Frederic Escourbiac, René Raffray, Philippe Chappuis, Takeshi Hirai, and Alex Martin. Overview and status of iter internal components. *Fusion engineering and design*, 89(7-8):890–895, Oct. 2014.

[26] Ch Linsmeier, M. Rieth, J. Aktaa, T. Chikada, A. Hoffmann, J. Hoffmann, A. Houben, H. Kurishita, X. Jin, M. Li, A. Litnovsky, S. Matsuo, A. von Müller, V. Nikolic, T. Palacios, R. Pippan, D. Qu, J. Reiser, J. Riesch, T. Shikama, R. Stieglitz, T. Weber, S. Wurster, J. H You, and Z. Zhou. Development of advanced high heat flux and plasma-facing materials. *Nuclear fusion*, 57(9):092007, Sep. 2017.

[27] John R. Rumble. *CRC handbook of chemistry and physics*. CRC Press, Taylor & Francis Group, Boca Raton ; London ; New York, 2017-2018, 98th edition edition, 2017.

[28] K. Schmid, J. Bauer, T. Schwarz-Selinger, S. Markelj, U. v. Toussaint, A. Manhard, and W. Jacob. Recent progress in the understanding of H transport and trapping in W. *Physica scripta*, T170:14037, Dec. 2017.

[29] Xunxiang Hu, Takaaki Koyanagi, Makoto Fukuda, N. A. P. Kiran Kumar, Lance L. Snead, Brian D. Wirth, and Yutai Katoh. Irradiation hardening of pure tungsten exposed to neutron irradiation. *Journal of nuclear materials*, 480:235–243, Nov. 2016.

[30] L. M. Garrison, Y. Katoh, and N. A. P. Kiran Kumar. Mechanical properties of single-crystal tungsten irradiated in a mixed spectrum fission reactor. *Journal of nuclear materials*, 518(C):208–225, May 2019.

[31] Alan Xu, Christian Beck, David E. J. Armstrong, Krishna Rajan, George D. W. Smith, Paul A. J. Bagot, and Steve G. Roberts. Ion-irradiation-induced clustering in w-re and w-re-os alloys: A comparative study using atom probe tomography and nanoindentation measurements. *Acta materialia*, 87:121–127, Apr. 2015.

[32] S. Wurster, N. Baluc, M. Battabyal, T. Crosby, J. Du, C. García-Rosales, A. Hasegawa, A. Hoffmann, A. Kimura, H. Kurishita, R. J. Kurtz, H. Li, S. Noh, J. Reiser, J. Riesch, M. Rieth, W. Setyawan, M. Walter, J. H You, and R. Pippan. Recent progress in R&D on tungsten alloys for divertor structural and plasma facing materials. *Journal of nuclear materials*, 442(1-3):S181–S189, Nov 2013.

[33] O. El-Atwani, J. A. Hinks, G. Greaves, J. P. Allain, and S. A. Maloy. Grain size threshold for enhanced irradiation resistance in nanocrystalline and ultrafine tungsten. *Materials research letters*, 5(5):343–349, Feb. 2017.

[34] J. W. Yeh, S. K. Chen, S. J. Lin, J. Y. Gan, T. S. Chin, T. T. Shun, C. H. Tsau, and S. Y. Chang. Nanostructured high-entropy alloys with multiple principal elements: Novel alloy design concepts and outcomes. *Advanced engineering materials*, 6(5):299–303, May. 2004.

[35] Stéphane Gorsse, Daniel B. Miracle, and Oleg N. Senkov. Mapping the world of complex concentrated alloys. *Acta materialia*, 135:177–187, Aug. 2017.

[36] B. Cantor, I. T. H. Chang, P. Knight, and A. J. B. Vincent. Microstructural development in equiatomic multicomponent alloys. *Materials science & engineering. A, Structural materials : properties, microstructure and processing*, 375-377:213–218, Jul. 2004.

[37] D. B. Miracle and O. N. Senkov. A critical review of high entropy alloys and related concepts. *Acta materialia*, 122:448–511, Jan. 2017.

[38] Jien-Wei Yeh. Recent progress in high-entropy alloys. *European journal of control*, 31(6):633–648, Dec. 2006.

[39] Jien Wei Yeh, Yu Liang Chen, Su Jien Lin, and Swe Kai Chen. High-entropy alloys - a new era of exploitation. *Materials science forum*, 560:1–9, Nov. 2007.

[40] Roksolana Kozak, Alla Sologubenko, and Walter Steurer. Single-phase high-entropy alloys - an overview. *Zeitschrift für Kristallographie. Crystalline materials*, 230(1):55–68, Jan. 2015.

[41] Yong Zhang, Ting Ting Zuo, Zhi Tang, Michael C. Gao, Karin A. Dahmen, Peter K. Liaw, and Zhao Ping Lu. Microstructures and properties of high-entropy alloys. *Progress in materials science*, 61:1–93, april 2014.

[42] E. P. George, W. A. Curtin, and C. C. Tasan. High entropy alloys: A focused review of mechanical properties and deformation mechanisms. *Acta Materialia*, 188:435–474, april 2020. ID: 271635.

[43] Yao Qiu, Sebastian Thomas, Mark A. Gibson, Hamish L. Fraser, and Nick Birbilis. Corrosion of high entropy alloys. *Npj Materials degradation*, 1(1), Aug. 2017.

[44] B. Gludovatz, A. Hohenwarter, D. Catoor, E. H. Chang, E. P. George, and R. O. Ritchie. A fracture-resistant high-entropy alloy for cryogenic applications. *Science (American Association for the Advancement of Science)*, 345(6201):1153–1158, Sep. 2014.

[45] Yu Zou, Huan Ma, and Ralph Spolenak. Ultrastrong ductile and stable high-entropy alloys at small scales. *Nature communications*, 6(1):7748, July 2015.

[46] Song qin Xia, Zhen Wang, Teng fei Yang, and Yong Zhang. Irradiation behavior in high entropy alloys. *Journal of iron and steel research, international*, 22(10):879–884, 2015.

[47] F. Wang, Y. Zhang, G. Chen, and H. A. Davies. Tensile and compressive mechanical behavior of a $CoCrCuFeNiAl_{0.5}$ high entropy alloy. *International journal of modern physics. B, Condensed matter physics, statistical physics, applied physics*, 23(6n07):1254–1259, Mar. 2009.

[48] X. F. Wang, Y. Zhang, Y. Qiao, and G. L. Chen. Novel microstructure and properties of multicomponent $CoCrCuFeNiTi_x$ alloys. *Intermetallics*, 15(3):357–362, Mar. 2007.

[49] Y. J. Zhou, Y. Zhang, Y. L. Wang, and G. L. Chen. Solid solution alloys of $AlCoCrFeNiTi_x$ with excellent room-temperature mechanical properties. *Applied physics letters*, 90(18):181904, Apr. 2007.

[50] Weidong Li, Peter K. Liaw, and Yanfei Gao. Fracture resistance of high entropy alloys: A review. *Intermetallics*, 99(C):69–83, Aug. 2018.

[51] Y. Y. Chen, T. Duval, U. D. Hung, J. W. Yeh, and H. C. Shih. Microstructure and electrochemical properties of high entropy alloys - a comparison with type-304 stainless steel. *Corrosion science*, 47(9):2257–2279, Sep. 2005.

[52] Y. Qiu, M. A. Gibson, H. L. Fraser, and N. Birbilis. Corrosion characteristics of high entropy alloys. *Materials science and technology*, 31(10):1235–1243, Mar. 2015.

[53] Oleg N. Senkov, Daniel B. Miracle, Kevin J. Chaput, and Jean-Philippe Couzinie. Development and exploration of refractory high entropy alloys - a review. *Journal of materials research*, 33(19):3092–3128, Oct. 2018.

[54] Y. Zou, P. Okle, H. Yu, T. Sumigawa, T. Kitamura, S. Maiti, W. Steurer, and R. Spolenak. Fracture properties of a refractory high-entropy alloy: In situ micro-cantilever and atom probe tomography studies. *Scripta materialia*, 128:95–99, Feb. 2017.

[55] E. Levo, F. Granberg, C. Fridlund, K. Nordlund, and F. Djurabekova. Radiation damage buildup and dislocation evolution in ni and equiatomic multicomponent ni-based alloys. *Journal of nuclear materials*, 490:323–332, July 2017.

[56] N. A. P. Kiran Kumar, C. Li, K. J. Leonard, H. Bei, and S. J. Zinkle. Microstructural stability and mechanical behavior of FeNiMnCr high entropy alloy under ion irradiation. *Acta materialia*, 113(C):230–244, July 2016.

[57] S. Abhaya, R. Rajaraman, S. Kalavathi, C. David, B. K. Panigrahi, and G. Amarendra. Effect of dose and post irradiation annealing in Ni implanted high entropy alloy FeCrCoNi using slow positron beam. *Journal of alloys and compounds*, 669:117–122, June 2016.

[58] K. Jin, C. Lu, L. M. Wang, J. Qu, W. J. Weber, Y. Zhang, and H. Bei. Effects of compositional complexity on the ion-irradiation induced swelling and hardening in Ni-containing equiatomic alloys. *Scripta materialia*, 119(C):65–70, July 2016.

[59] Yiping Lu, Hefei Huang, Xuzhou Gao, Cuilan Ren, Jie Gao, Huanzhi Zhang, Shijian Zheng, Qianqian Jin, Yonghao Zhao, Chenyang Lu, Tongmin Wang, and Tingju Li. A promising new class of irradiation tolerant materials: $Ti_2ZrHfV_{0.5}Mo_{0.2}$ high-entropy alloy. *Journal of materials science & technology*, 35(3):369–373, Mar. 2019.

[60] Dhinisa Patel, Mark D. Richardson, Bethany Jim, Shavkat Akhmadaliev, Russell Goodall, and Amy S. Gandy. Radiation damage tolerance of a novel metastable refractory high entropy alloy $V_{2.5}Cr_{1.2}WMoCo_{0.04}$. *Journal of nuclear materials*, 531:152005, Apr. 2020.

[61] Gui-Yang Huang, Niklas Juslin, and Brian D. Wirth. First-principles study of vacancy, interstitial, noble gas atom interstitial and vacancy clusters in bcc-W. *Computational materials science*, 123(C):121–130, Oct. 2016.

[62] Lawrie Lloyd. *Handbook of Industrial Catalysts*. Springer, New York, NY, 2011.

[63] Andrew R. Leach. *Molecular modelling : principles and applications*. Prentice Hall, Harlow, England; New York, 2001. ID: 45008511.

[64] Sam McArdle, Suguru Endo, Alán Aspuru-Guzik, Simon C. Benjamin, and Xiao Yuan. Quantum computational chemistry. *Reviews of modern physics*, 92(1), Mar. 2020.

[65] Peter Atkins and Ronald Friedman. *Molecular quantum mechanics*. Oxford University Press, Oxford, 5 edition, 2011. ID: alma9927245253506253.

[66] P. Hohenberg and W. Kohn. Inhomogeneous electron gas. *Physical Review*, 136(3):B864–B871, 1964. ID: 10.1103/PhysRev.136.B864; J1: PR.

[67] W. Kohn and L. J. Sham. Self-consistent equations including exchange and correlation effects. *Physical review*, 140(4A):A1133–A1138, Nov. 1965.

[68] G. Kresse and J. Furthmüller. Efficient iterative schemes for ab initio total-energy calculations using a plane-wave basis set. *Physical review. B, Condensed matter*, 54(16):11169–11186, Oct. 1996.

[69] P. E. Blöchl. Projector augmented-wave method. *Phys. Rev. B*, 50:17953–17979, Dec. 1994.

[70] Kamal Choudhary, Faical Yannick P. Congo, Tao Liang, Chandler Becker, Richard G. Hennig, and Francesca Tavazza. Evaluation and comparison of classical interatomic potentials through a user-friendly interactive web-interface. *Scientific data*, 4(1):160125, Jan. 2017.

[71] Wikipedia, the free encyclopedia: Molecular dynamics. https://en.wikipedia.org/w/index.php?title=Molecular_dynamics&oldid=998332920, 2021.

[72] J. E. Jones. On the Determination of Molecular Fields. II. From the Equation of State of a Gas. *Proceedings of the Royal Society of London Series A*, 106(738):463–477, oct. 1924.

[73] R. A. Buckingham. The classical equation of state of gaseous helium, neon and argon. *Proceedings of the Royal Society of London. Series A, Mathematical and physical sciences*, 168(933):264–283, Oct. 1938.

[74] Philip M. Morse. Diatomic molecules according to the wave mechanics. ii. vibrational levels. *Physical review*, 34(1):57–64, Jul. 1929.

[75] James F. Ziegler, Jochen P. Biersack, and U. Littmark. *The stopping and range of ions in solids*, volume 1. Pergamon Pr, New York [u.a.], 1985.

[76] J. K. Nørskov. Covalent effects in the effective-medium theory of chemical binding: Hydrogen heats of solution in the 3d metals. *Physical review. B, Condensed matter*, 26(6):2875–2885, sep. 1982.

[77] M. J. Stott and E. Zaremba. Quasiatoms: An approach to atoms in nonuniform electronic systems. *Physical review. B, Condensed matter*, 22(4):1564–1583, Aug. 1980.

[78] Murray S. Daw and M. I. Baskes. Embedded-atom method: Derivation and application to impurities, surfaces, and other defects in metals. *Physical Review B*, 29(12):6443–6453, 1984. ID: 10.1103/PhysRevB.29.6443; J1: PRB.

[79] Murray S. Daw, Stephen M. Foiles, and Michael I. Baskes. The embedded-atom method: a review of theory and applications. *Materials science reports*, 9(7-8):251–310, mar. 1993.

[80] M. I. Baskes. Modified embedded-atom potentials for cubic materials and impurities. *Physical review. B, Condensed matter*, 46(5):2727–2742, Aug. 1992.

[81] Frank H. Stillinger and Thomas A. Weber. Computer simulation of local order in condensed phases of silicon. *Physical review. B, Condensed matter*, 31(8):5262–5271, April 1985.

[82] G. C. Abell. Empirical chemical pseudopotential theory of molecular and metallic bonding. *Physical review B, Condensed matter*, 31(10):6184–6196, May 1985.

[83] J. Tersoff. New empirical approach for the structure and energy of covalent systems. *Physical Review B*, 37(12):6991–7000, 1988. ID: 10.1103/PhysRevB.37.6991; J1: PRB.

[84] Adri C. T van Duin, Siddharth Dasgupta, Francois Lorant, and William A. Goddard. ReaxFF: A reactive force field for hydrocarbons. *The journal of physical chemistry. A, Molecules, spectroscopy, kinetics, environment, & general theory*, 105(41):9396–9409, Oct. 2001.

[85] D. Pettifor. New many-body potential for the bond order. *Physical review letters*, 63(22):2480–2483, Nov. 1989.

[86] M. Aoki, A. Horsfield, and D. Pettifor. Tight-binding bond order potential a forces for atomistic simulations. *Journal of Phase Equilibria*, 18(6):614–623, Dec. 1997.

[87] Jörg Behler and Michele Parrinello. Generalized neural-network representation of high-dimensional potential-energy surfaces. *Physical review letters*, 98(14):146401, Apr. 2007.

[88] Albert P. Bartók and Gábor Csányi. Gaussian approximation potentials: A brief tutorial introduction. *International Journal of Quantum Chemistry*, 115(16):1051–1057, Aug. 2015.

[89] J. Byggmästar, K. Nordlund, and F. Djurabekova. Gaussian approximation potentials for body-centered-cubic transition metals. *Phys. Rev. Materials*, 4:093802, Sep. 2020.

[90] Carl Edward Rasmussen and Christopher K. Williams. *Gaussian Processes for Machine Learning*. MIT Press, Cambridge, MA, USA, 2005.

[91] David J. C. MacKay. *Information theory, inference, and learning algorithms*. Cambridge Univ. Press, Cambridge ; New York, NY, 4th print. edition, 2003.

[92] Albert P. Bartók, Risi Kondor, and Gábor Csányi. On representing chemical environments. *Physical Review B*, 87(18), May 2013.

[93] Albert P. Bartók, James Kermode, Noam Bernstein, and Gábor Csányi. Machine learning a general-purpose interatomic potential for silicon. *Physical review. X*, 8(4):041048, Dec. 2018.

[94] Albert Bartók-Pártay. *Gaussian approximation potential : an interatomic potential derived from first principles Quantum Mechanics*. PhD thesis, University of Cambridge, 2010.

[95] Ask Hjorth Larsen, Jens Jørgen Mortensen, Jakob Blomqvist, Ivano E. Castelli, Rune Christensen, Marcin Du ak, Jesper Friis, Michael N. Groves, Bjørk Hammer, Cory Hargus, Eric D. Hermes, Paul C. Jennings, Peter Bjerre Jensen, James Kermode, John R. Kitchin, Esben Leonhard Kolsbjerg, Joseph Kubal, Kristen Kaasbjerg, Steen Lysgaard, Jón Bergmann Maronsson, Tristan Maxson, Thomas Olsen, Lars Pastewka, Andrew Peterson, Carsten Rostgaard, Jakob Schiøtz, Ole Schütt, Mikkel Strange, Kristian S. Thygesen, Tejs Vegge, Lasse Vilhelmsen, Michael Walter, Zhenhua Zeng, and Karsten W. Jacobsen. The atomic simulation environment-a python library for working with atoms. *Journal of physics. Condensed matter*, 29(27):273002, June 2017.

[96] John P. Perdew, Kieron Burke, and Matthias Ernzerhof. Generalized gradient approximation made simple [phys. rev. lett. 77, 3865 (1996)]. *Physical review letters*, 78(7):1396, Feb. 1997.

[97] Hendrik J. Monkhorst and James D. Pack. Special points for brillouin-zone integrations. *Physical review. B, Solid state*, 13(12):5188–5192, June 1976.

[98] K. Nordlund, N. Runeberg, and D. Sundholm. Repulsive interatomic potentials calculated using hartree-fock and density-functional theory methods. *Nuclear instruments & methods in physics research. Section B, Beam interactions with materials and atoms*, 132(1):45–54, Oct. 1997.

[99] QUIP. https://github.com/libAtoms/QUIP, 2020.

[100] LAMMPS. https://lammps.sandia.gov/, 2020.

[101] Steve Plimpton. Fast parallel algorithms for short-range molecular dynamics. *Journal of computational physics*, 117(1):1–19, 1995.